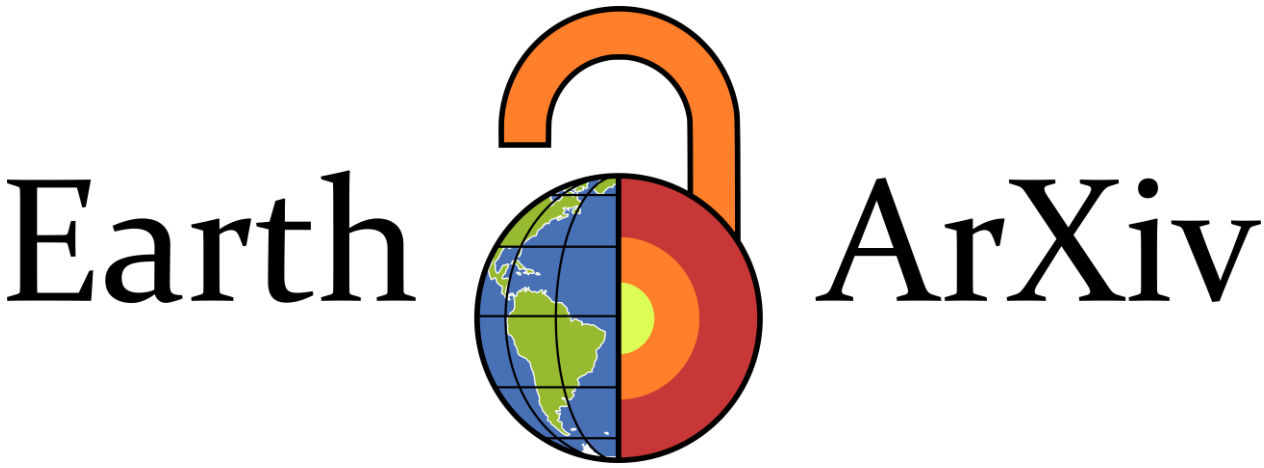

This manuscript has been published in *Proceedings of the Royal Society A*. The published version is available at:
https://doi.org/10.1098/rspa.2025.0733

PROCEEDINGS A

royalsocietypublishing.org/journal/rspa

Research

Article submitted to journal

Subject Areas:
fluid mechanics, geophysics

Keywords:
megadyke, mantle, plume, radial, neutral, buoyancy, fracture, flow, solidification, magma

Author for correspondence:
Tim Davis
e-mail: timothy.davis@bristol.ac.uk

Megadyke propagation down dynamic topography

Tim Davis[1,2], Yuan Li[2], Adina E. Pusok[2] and Richard F. Katz[2]

[1]School of Earth Sciences, Queens Rd, Bristol, BS8 1RJ, UK.

[2]Department of Earth Sciences, South Parks Road, Oxford, OX1 3AN, UK.

Magmatic dykes that align vertically and extend laterally for hundreds to thousands of kilometres are known as megadykes. Observations of solidified megadyke swarms indicate that they have a common magma source and a characteristic run-out length. There is no consensus on what determines this length. We develop quantitative predictions to test the hypothesis that run-out length is set by the dimensions of the topographic swell above a mantle plume.

Our model describes lateral dyke propagation from a constant-pressure magma source by fluid-driven fracturing of an elastic crust. The dyke is confined at its level of neutral buoyancy, which is warped by the dynamic topography of the plume swell. This gives the dyke gravitational potential energy that drives lateral magmatic flow. Solidification blocks the fracture perimeter when advance of the fracture's tip slows below a critical value.

When assisted by dynamic topography, dykes in this model propagate to lengths approximately twice the underlying plume-head radius. Hence our model links the characteristic dyke length of a megadyke swarm to the size of the ancient plume that created it. Furthermore, the model predicts a sensitivity to source pressure, explaining the existence of dykes that are far longer than others in a swarm.

THE ROYAL SOCIETY PUBLISHING

1. Introduction

A dyke is a planar, magma-filled fracture that transports magma through brittle rock. Magma flows between the walls of the crack, which extends as its tip propagates through intact rock. Radial megadyke swarms are clusters of large, laterally propagating dykes that are inferred to share the same magma source. The individual dykes can reach lengths of up to 4000 km, with typical lengths around 300 km, and widths between 10 and 100 m [1]. These colossal geological structures are observed in a solidified state on other planetary bodies including Venus (shown in Figure 1), Mars, Mercury and Earth [2]. The conditions and mechanics of their formation are enigmatic, particularly where they occur in the absence of plate tectonics [3].

Figure 1. Radial graben systems on Venus. **Panel a** shows a histogram of maximum graben lengths from detailed mapping [4,5]. **Panel b** shows a schematic of radiating graben–fissure systems in the Guinevere Planitia and Beta Region, Venus. These are interpreted as the surface expressions of dykes. The map is displayed in a sinusoidal projection with the central meridian at 294°. Adapted from Ernst *et al.* [4] and Ernst [2].

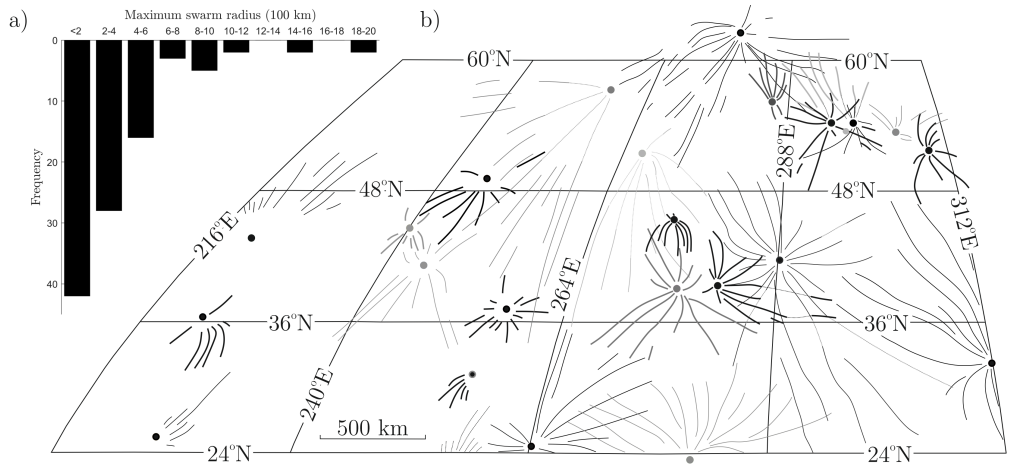

The observational study of radial megadyke swarms has evolved significantly since their initial identification. While early studies documented their characteristics, e.g., Fahrig & Jones [6], it was not until the early 1980s that their genesis became a topic of research [7]. Henry Halls' pivotal work challenged the prevailing assumption of predominantly vertical magma flow in dykes, emphasising the potential for lateral emplacement [8]. This shift in perspective led to international conferences and the first global compilation of megadyke swarms, published in the mid-'80s and early '90s [9,10]. Soon after, compelling evidence from magnetic-fabric studies of megadykes confirmed that lateral magma flow within the dyke, rather than vertical, was the primary emplacement mechanism [11]. This modern understanding is supported by the uniform chemistry and the spoke-like arrangement of megadyke swarms [12].

Around the same time that lateral propagation was recognised, space missions extended the identification of swarms beyond Earth. The Magellan mission in the early 1990s provided radar images of most of Venus' surface with a resolution of ∼100 m. This enabled the detection of graben systems radiating hundreds to thousands of km from central sources, as mapped in Fig. 1. Moreover, the negligible erosion that has occurred post-emplacement on other planets afforded an unaltered view of their structural characteristics [4,5,13]. Observations of lava flows and minor volcanic shields and cones associated with these grabens are conclusive evidence that they are the surface expressions of dykes [14]. This evidence is bolstered by their structural similarity to grabens overlying buried megadykes on Earth, e.g. [15]. Moreover, mechanical theory shows that

dyke emplacement beneath a free surface induces graben formation through stress changes [16], and that the graben geometry can be used to constrain dyke dimensions and depth.

The discovery of extraterrestrial megadykes confirmed that the processes responsible for megadyke formation are not unique to Earth. In particular, it taught us that megadyke swarms can occur in the absence of plate tectonics. However, numerous questions arise on the basis of the assembled observations of megadyke swarms. We highlight the following, which we consider to be of leading-order importance.

- If a large source pressure, in excess of lithostatic, were required to overcome viscous drag and drive dykes great distances, why would this same overpressure not instead drive magma upward through the free surface?
- What sets the distance at which a laterally propagating dyke will stop? Are run-out lengths limited by the magma-chamber volume? Are they limited by magma solidification? What is the role of gravitational potential energy in driving dyke propagation?
- Why do the majority of megadykes of a single swarm exhibit similar lengths (e.g., Fig. 1)?
- Is magmatic flow in megadykes turbulent? If so, how does this influence run-out length?

Some of these questions have been raised and addressed by previous studies that we review below. Our aim in this work is to derive a consistent theory that captures the essential physics of megadykes and answers all the above questions.

(a) Review of theories and constraints on lateral dyke propagation

There are numerous studies describing well-established mechanisms that create the angular spacing and surface patterns of radial, fluid-driven cracks propagating from a pressurised source [13,17–19]. Models show that laterally propagating dykes are not required to be connected to a magma chamber at the same depth. Instead, such dykes may first buoyantly ascend from a deeper source to their Level of Neutral Buoyancy (LNB), and only transition to lateral propagation at this shallower level [20–23]. Various authors have hypothesised that this lateral propagation is promoted by a surface slope associated with dynamic topography [1,24–26]. Topographic uplift results in an inclined LNB, causing magma contained in the dyke to flow downslope. This slope promotes higher flow speeds that, in turn, reduce the propensity for solidification and arrest of the dyke. Ernst & Buchan [27] suggest that the plume size (and hence radius of dynamic surface uplift) controls the characteristic radius of the swarm. The dynamics underlying this hypothesis have not been quantified and hence remain untested.

Widely cited three-dimensional (3D) models of laterally propagating dykes neglect surface uplift entirely, but build a framework into which uplift may be added [19,28]. Bolchover & Lister [28] consider a dyke perched within a crust of varying density at its level of neutral buoyancy, driven laterally by a constant pressure at the magma source. Their model includes magma solidification and hence a critical tip speed below which propagation ceases (we review solidification in dyke models below). This enables predictions of final dyke lengths. The predicted lengths are highly sensitive to the source pressure. Bunger *et al.* [19] use models developed for industrial applications to predict lateral propagation speed. They show that this speed decreases with time as $t^{-1/2}$ for a constant pressure at the source.

Other workers have developed simplified theories for lateral propagation driven by sloped surface uplift. McKenzie *et al.* [24] assume a constant volume-rate of flow through a fixed-width channel that is inclined at an angle. They include an empirical relation for turbulent drag and show that the dyke propagates at a constant speed. Substituting reasonable physical parameters, they estimate this speed as $\sim 3\ \mathrm{m\ s^{-1}}$, consistent with observations of laterally propagating dykes. Fialko & Rubin [25] also consider a dyke propagating laterally down a gentle, uniform slope. This terminates at a point where magma breaches the surface and erupts. They argue (but do not show) that this terminus would tend to occur where the surface slope vanishes, implicitly predicting

that the dyke reaches a length determined by the uplift shape. It is of note that few megadykes are observed to have eruptions at their terminus [4].

Predictions of the length over which a dyke can propagate laterally must be based on a mechanism by which propagation ceases. There are two relevant hypotheses here. The first is that propagation ceases when the magma-source pressure or volume is depleted by evacuation into the dyke. The second is that propagation ceases when the fluid channel is fully blocked by solidified magma. We consider each of these in turn.

Observations of megadykes suggest that magma is predominantly supplied from the lower crust or upper mantle. This is seen in data from the Mackenzie swarm in Canada, where the transition from vertical to lateral flow typically occurs at substantial radial distances from the swarm's focal point. Vertical flow from a lower source is observed as far as 500 km away in the Mackenzie swarm [11].

Geodetic observations of modern volcanic systems typically indicate stacked and coupled magma sills, comprising a shallow, upper crustal reservoir fed by a deeper reservoir. The upper crustal reservoir feeds dyke propagation [29]. Near megadyke arrays, evidence for these upper crustal reservoirs is preserved in collapse structures that form depressions. However, dyke propagation does not cease at the time when the upper-crustal reservoir volume is depleted [3]. To illustrate this latter point, we use observations to assess whether the depression associated with collapse of the upper-crustal reservoir feeding a swarm of megadykes has a volume comparable to one of the observed dykes. If these volumes are similar, then run-out would plausibly be limited by magma supply in the upper reservoir.

Ernst *et al*. [4], in their Table 1, provide the lengths of four large radial dyke swarms on Venus and the area of the collapse structures overlying the site of magma withdrawal. Krassilnikov [30] shows that the typical surface depression of the collapse structures is 1 km, enabling an estimate of their volume. Following the method of McKenzie & McKenzie [24], to estimate the volume of a characteristic dyke in the swarm and hence the volume of magma withdrawn from the reservoir to feed it, we calculated these volumes for the four cases reported in both studies (R15, R21, R23, and R31). In all cases examined, the withdrawn volume is an order of magnitude smaller than the reservoir volume. A discrepancy is evident in the case of the longest dyke in the solar system, where the volume of the associated collapse structure is much smaller than that of the dyke itself [3]. If this comparison holds true in general, it indicates that megadyke run-out is not limited by the upper-crustal magma-reservoir volume, but rather is fed by deeper sources.

These observations suggest that megadykes are predominantly fed by sources from below, and for these dykes, depletion of upper-crustal-reservoir volumes does not cause propagation to cease (i.e., megadykes do not seem to exhaust the source). Moreover, outlier dykes with far larger lengths are seen in many swarms, demonstrating that the average dyke sizes within a given radial swarm are not constrained by magma supply limitations, since the same source can generate dykes with significantly greater volumes than the majority of observable dykes in that swarm.

Solidification is the second candidate mechanism for dyke arrest. In principle, it could operate by blocking magma flow in the tail of the dyke, or by blocking propagation of the tip. However, it is well established that solidification will not block dyke tails that have a width of $\sim$10 m or more [25,31]. In such cases, advective heat transport vastly exceeds diffusive loss into the host rock.

Solidification at the dyke tip appears to be the most plausible mechanism for dyke arrest. This occurs when the rate at which the dyke walls open is less than the rate at which they close by solidification. Since the tip opening rate is directly proportional to the tip propagation speed, this mechanism will arrest any part of the propagating dyke's tip-line that drops below a certain speed. Physical models robustly predict that tip speed will decrease with time (or distance from the source) [19,32–34], but various thermal and mechanical factors control the time at which freeze-over occurs. These factors can be analysed by combining asymptotic analysis of tip-opening mechanics, e.g., [35,36] with a solution of the moving boundary problem of

pure-phase solidification [28,37]. This enables the derivation of a critical speed below which propagation is blocked—a stopping criterion. In the absence of an increase in fluid pressure at the tip, propagation of the tip cannot restart.

While this analysis is internally consistent, observations show that natural and experimental fluid-filled fractures exhibit start–stop behaviour [38–40]. This complexity may arise from heterogeneity in the solid medium and/or unsteady dynamics of fluid flow when solidification dominates. It seems reasonable to assume that a solidification criterion provides a good approximation of the time-averaged behaviour of a dyke under unsteady propagation.

The theory reviewed above goes part of the way toward a quantitative understanding of megadykes, but does not fully address the questions that we highlighted. In particular, in the theory without surface uplift, large source pressure is required to explain dyke length. But in this case, we would expect near-source eruption to preclude lateral propagation. Moreover, assuming that near-source eruption does not occur, the sensitivity of run-out length to source pressure makes it difficult to explain why dykes within a single swarm have similar lengths [28]. For the theory that includes uplift, no model for run-out length exists. In this context, we still lack the ability to interpret the mean length of dykes in a swarm in terms of source parameters.

Here we develop quantitative predictions of dyke length in a model that includes domal topographic uplift, turbulent flow, and magma solidification. Following Bolchover & Lister [28], our theory describes a pseudo-3D, fluid-filled fracture that can propagate vertically and laterally [41]. We obtain numerical solutions and use scaling analysis to verify these and to explain their properties. Our results support the hypothesis that dynamic topographic uplift is a key control on mean dyke length in swarms, and can hence be inferred from observations. Before developing the theory, we next outline the key physical considerations that underpin it.

(b) Preliminary discussion of relevant physical properties and processes

A model of a laterally propagating dyke, fed by an inexhaustible, constant-pressure source, must incorporate a minimum set of physical processes to address the questions above. It must capture the elastic deformation of the host rock around the dyke and the flow of magma within it, including the effect of the gravitational body force. It must balance the magma pressure with elastic stress, normal to the dyke wall. It must capture the advance of the dyke tip by mode-I fracture around the full perimeter of the dyke. And it must capture the closure of the dyke aperture and tip blocking by magma solidification onto the walls. It is, of course, possible to add further physical complexity to a model, but here and in previous work, these are considered the fundamental aspects of lateral dyke propagation [28,35].

Lateral propagation of the dyke is not guaranteed to occur in a model that includes these features, however. It depends on one other crucial point: the density structure of the crust through which the dyke propagates. This structure must be such that the magma finds a level of neutral buoyancy at which it is stable and does not breach the surface [23,42]. If this level extends laterally, the magma can follow it by doing work to create new fracture surface, push apart the walls, and flow viscously into the opening. The energy needed for this is derived from the magma pressure of the source and the gravitational potential energy associated with uplift of the LNB. Because the LNB maintains a constant depth below the surface, the weight of the rock overlying it is everywhere the same, regardless of uplift. However, the uplift introduces a slope to the surface (and the LNB), and hence creates a lateral gradient of gravitational potential energy. To convert this potential energy to work within the dyke, magma propagates down-slope along the LNB.

Based on these considerations, we aim to develop a theory that makes quantitative predictions of dyke run-out length. However, qualitative predictions are accessible even at this stage. We readily anticipate that larger source pressure and greater LNB relief lead to larger run-out. Denser magma has greater potential energy per unit of uplift and will propagate faster and further down slope. Faster solidification will block tip propagation at higher speeds, reducing the run-out length. Counter-intuitively, greater fracture toughness promotes run-out by requiring a wider aperture at the tip, and hence inhibiting tip blockage by solidification. Greater elastic stiffness

of wall rock reduces the width of both tip and tail of the dyke, restricting magma supply and diminishing run-out length. Larger magma viscosity also restricts magma supply. Our theory is designed to quantify these sensitivities, predict dyke length as a function of uplift parameters, and hence clarify how dynamic topography controls the characteristics of megadyke swarms on Earth and other bodies.

(c) Structure of the manuscript

The manuscript is arranged as follows. In section 2, we discuss the relevant physics and derive governing equations for a pseudo-3D, laterally propagating dyke. While the pseudo-3D model captures the dynamics of 3D dyke propagation, it is expressed mathematically in a simplified 2D form. In section 3, we present results of numerical solutions to our pseudo-3D formulation. We first model dykes driven solely by source pressure (without uplift), and investigate the role of pressure, turbulence and solidification on run-out length. We then incorporate a simple model of domal uplift above a hotspot swell and examine its consequences. For cases with and without uplift, we use scaling analysis to understand parametric controls. Section 4 reviews and discusses our models, and makes preliminary comparisons with observations. Section 5 summarises the key outcomes of our work, draws conclusions and raises questions for further research.

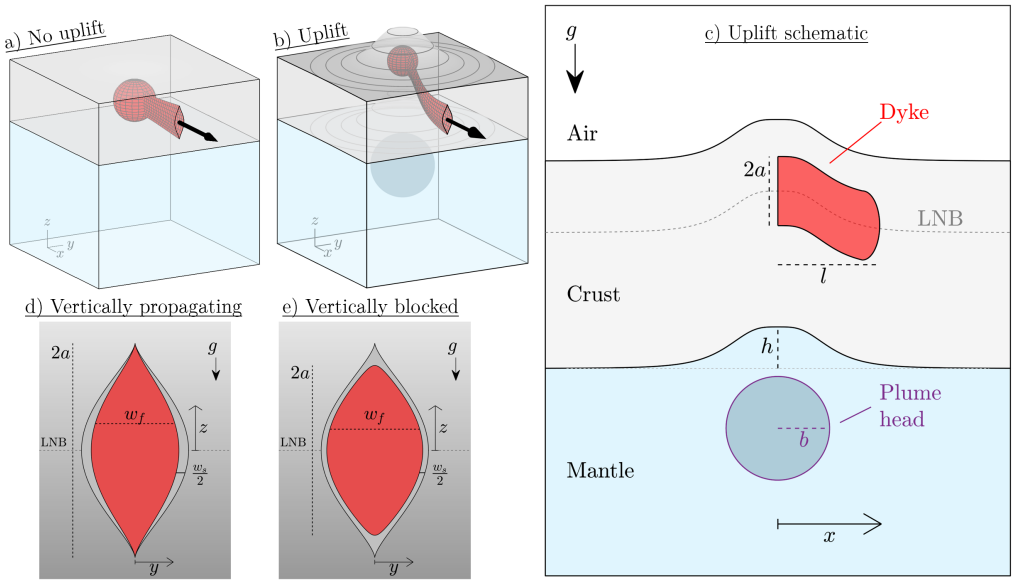

Figure 2. Schematic diagrams of the model (not to scale). **Panel a** presents a three-dimensional view of a dyke propagating laterally away from a pressurised source, cutting through the grey-coloured crust. In **panel b**, a rising plume head uplifts and warps the crust. **Panel c** shows an x–z cross-section through panel b, with key lengths indicated. Note the deflection of the level of neutral buoyancy. **Panels d** and **e** depict y–z cross-sections of the dyke in a crust of linearly increasing density (deepening shade of grey). The pressurised fluid magma that opens the walls of the dyke is indicated in red and the solidified magma on the walls, which has the same density as the host rock at the LNB, is shown in grey.

2. Assembling a theory of megadyke dynamics

Here we introduce the essential geometry and physics, and assemble a mathematical framework to approximate it. Figure 2 shows schematic diagrams of the model. The 3D diagrams in panels a and b place the dyke into a Cartesian coordinate system. We choose Cartesian over cylindrical

coordinates because the planar dyke geometry is more naturally represented in Cartesian form, with the source at $x = 0$ corresponding to the centre $r = 0$ of any radially symmetric topography, and the lateral propagation direction x aligning with the radial coordinate. The z direction is upward, opposite to the gravity force per unit mass $\boldsymbol{g}$. The dyke propagates laterally in the x direction but its upper and lower tip-lines propagate vertically—that is, the top of the dyke moves upward (positive z) and the bottom moves downward (negative z). The y direction is across the dyke, in the direction of wall opening. Panels b and c show the surface uplift pattern $h(x)$ that we impose, where h_0 defines the maximum vertical uplift and b defines the horizontal extent (the analytical form is given below). We require that any dynamic topography, shown in panels b and c, has a surface slope of order $h_0/b \ll 1$. Hence we approximate that x measures distance along the dyke centreline, which is always at $z = 0$, regardless of uplift.

The dyke extends from $x = 0$ to the location of its lateral tip line, $x = l(t)$. Its speed is defined by $v(x = l) \equiv \mathrm{d}l/\mathrm{d}t$, the rate at which the tip moves laterally. The dyke has a half-height a, such that the vertical tip-lines are located at $z = \pm a(x, t)$. The dyke is filled with fluid to a width w_f with walls at $y = \pm w_f(x, z, t)/2$, beyond which is solidified magma with thickness $w_s(x, z, t)/2$. Hence the full opening of the host rock is $w(x, z, t) = w_f + w_s$, as shown in panel d. Panel e shows that the upper and lower tip-lines can become blocked by solidification, in which case $w(x, \pm a, t) = w_s(x, \pm a, t) > 0$. For typical megadykes on Earth, characteristic dimensions are $l \sim$ 300 km, $a \sim 20$ km and $w \sim 10$ m [1].

The three-dimensional shape of a laterally propagating dyke is such that $l \gg a \gg w$, except at very early times. We exploit this separation of scales to introduce lubrication theory and the pseudo-3D approximation following, e.g., Adachi *et al.* [41]. At each position x, we treat the elastic problem of wall opening as being an independent, two-dimensional problem in the y–z plane. This is illustrated by the vertical cross-sections in Fig. 2d and e. Furthermore, by integrating across the width of the dyke, we treat the viscous problem of lateral magma flow as being a two-dimensional problem in the x–z plane as in panel c. These two problems are coupled via the excess pressure $p(x, z, t)$—the magma pressure in excess of the pre-dyking least compressive stress at the LNB—this stress is assumed to be uniform in y.

An important feature of this framework is that each vertical cross-section can exist in one of two states, as shown in Fig. 2d and e. In the first state, fluid drives the dyke tips vertically into unfractured crust (panel d). Alternatively, once solidification blocks the dyke tips (panel e), the fluid-filled region recedes from the arrested crack boundaries.

The dyke is embedded in the host rock of the crust, which has a density ρ_r that increases linearly with depth,

$$\rho_r = \rho_f - Rz, \tag{2.1}$$

where ρ_f is the density of the magma in the dyke, z is height above the centreline of the dyke, and $R > 0$ is a constant that sets the crustal density variation. In the Canadian shield, estimates of R from seismic velocity studies are around 0.02 kg m^{-4} [43]. A typical estimate for the density of solidified magma in megadykes is around $\rho_f = 3000$ kg m^{-3} e.g., [12].

The dyke is connected to a magma source at $x = 0$, which maintains a constant overpressure (pressure in excess of the lithostatic, least-compressive stress) given by p_0, which we treat as a constant. Whilst pressures at the source of megadykes are poorly known, a representative value could be around 5 MPa [44].

Propagation of the tip-line, whether vertical or lateral, requires that the stress intensity at the tip exceeds a threshold. We assume a critical stress intensity for mode-I (opening mode) failure K_c that is uniform in time and space. A typical value for K_c is 5 MPa m$^{1/2}$ [23]. Where the tip has been blocked by solidification (a situation we discuss below), it can no longer advance into the unfractured rock ahead [28].

(a) Cross-section of a dyke perched at its level of neutral buoyancy

We choose our coordinate system such that the LNB is located at $z = 0$, which corresponds to the reference level for the linear vertical density profile of the host rock given in equation (2.1). The fluid pressure in excess of the lithostatic pressure is the force per unit area that holds apart the walls of the dyke. This excess pressure is the sum of two contributions: a dynamic part $p_f(x,t)$ that varies in x along the centreline and a static part related to the crustal density gradient that varies in z. The excess pressure is thus

$$p(x,z,t) = p_f(x,t) - Rgz^2/2. \tag{2.2}$$

At some finite time and for a particular value of $0 < x < l(t)$, the excess pressure has a vertical distribution $p(z)$. An exact solution for this pressure distribution assuming plane-strain conditions is given by superposition of solutions 5.10a of Tada *et al.* [45] (p. 139). The pressure pushes open the dyke walls, which creates an opening-mode stress intensity K_I at $z = \pm a$ given by

$$K_I(x, z = \pm a, t) = \frac{1}{(\pi a)^{1/2}} \int_{-a}^{a} p(x,\xi,t) \frac{\left(a^2 - \xi^2\right)^{1/2}}{a \mp \xi} \, \mathrm{d}\xi, \tag{2.3}$$

The value of $a(x,t)$ is determined such that $K_I(z = \pm a) = K_c$, unless the upper and lower tips are blocked by solidified magma. The associated opening profile is given by

$$w_f(x,z,t) = \frac{4}{\pi E'} \int_{-a}^{a} p(x,\xi,t) \cosh^{-1}\left(\frac{a^2 - \xi z}{a|z - \xi|}\right) \mathrm{d}\xi, \tag{2.4}$$

where the plane strain modulus $E' \equiv E/(1-\nu^2)$ contains Young's modulus E and Poisson's ratio ν. The area of this aperture is given by

$$A_f(x,t) = \frac{4}{E'} \int_{-a}^{a} p(x,\xi,t) \left(a^2 - \xi^2\right)^{1/2} \mathrm{d}\xi. \tag{2.5}$$

As with w, the cross-sectional area A is the sum of the fluid and solid parts, $A(x,t) = A_f + A_s$. We detail the equations describing solid widths w_s and areas A_s later, in Section 2(e).i. Closure requires coupling with the fluid dynamics to constrain A_f and solidification to constrain A_s.

(b) Lateral magma flow through the dyke

The separation of scales associated with dyke geometry encourages us to make a lubrication approximation where the magma velocity is non-zero only in the x direction. For laminar flow, this gives rise to a classical Poiseuille velocity field that is readily integrated in y across the width of the dyke. For turbulent flow, lubrication theory is not strictly valid. However, recognising that the maximum scale of turbulence must be smaller than the minimum dyke dimension (dyke width), we can rely on an empirical parameterisation [46]. The Darcy-Weisbach equation is a general expression for the width-integrated flow q (units of m^2/s) that accommodates both laminar and turbulent cases,

$$q(x,z,t) = \left[\left(\frac{\partial p}{\partial x} + \rho_f g \frac{\partial h}{\partial x} \right) \frac{4 w_f^3}{\rho_f} \frac{1}{F\left(\frac{4}{3}Re, \frac{w_R}{w_f}\right)} \right]^{1/2}, \tag{2.6}$$

Flow is driven by the lateral pressure gradient and the component of gravity down the (small) slope of the topography $h(x)$. The second term $\rho_f g \, \partial h/\partial x$ arises from the small tilt of the x-axis with respect to the horizontal, because it conforms to the dynamic topography. At low slope angles γ, $\partial h/\partial x = \sin\gamma \simeq \gamma$, is used to approximate the gravitational component along the topographic slope. The effect of turbulent dissipation is captured by a dimensionless, modified

Fanning factor F [47,48], a function of the Reynolds number,

$$Re \equiv 24 \frac{\rho_f q}{\eta'}, \tag{2.7}$$

and the scale of wall roughness w_R relative to the dyke fluid width w_f.

At small *Re* associated with laminar flow, the Fanning factor is $F \sim 96/Re$. Substituting this into (2.6) results in the familiar lubrication equation for flux through a narrow slot, $q = (w_f^3 \partial \bar{p}/\partial x)/\eta'$, where $\eta' \equiv 12\eta$ [48,49]. Here, to simplify notation, we have defined $\partial \bar{p}/\partial x$ as the centreline pressure gradient given by the quantity in brackets in eqn. (2.6). At large *Re* associated with turbulent flow, the dependence of the Fanning factor on q makes equation (2.6) nonlinear. In supplementary material section S.1 we describe how root finding is used to resolve this non-linearity.

The rate of volume transport $Q(x,t)$ through a cross-section of the dyke is given by integrating $q(x,z,t)$ over the dyke height

$$Q(x,t) = \int_{-a}^{a} q \, \mathrm{d}z. \tag{2.8}$$

The mean cross-sectional fluid velocity in the dyke can then be defined as

$$v(x,t) \equiv Q/A_f. \tag{2.9}$$

Variation in time of the cross-sectional area A_f is associated, by conservation of mass, with the divergence of Q. With the assumption of constant magma density, and anticipating a slow loss of magma to solidification, we can derive a volume-conservation statement,

$$\frac{\partial A_f}{\partial t} + \frac{\partial A_s}{\partial t} + \frac{\partial Q}{\partial x} = 0. \tag{2.10}$$

This equation couples the dyke's fluid-filled cross-sectional area A_f, controlled by fluid pressure via (2.5), to the volume rate Q that is controlled by the pressure gradient via equations (2.6) and (2.8). We next discuss the topographic profile h and define the area of solidified magma A_s in section 2(e).i.

(c) A simple model of dynamic topography

In equation (2.6), flow through the dyke is driven partly by the topographic gradient $\partial h/\partial x$. This coupling reflects the assumption that the LNB is warped to follow the ground surface of dynamic topography above a rising mantle plume, as illustrated in Figure 2c. Uplift of the LNB furnishes the dyke with gravitational potential energy, which it expends by lateral propagation down the topographic gradient.

We employ a model of dynamic topography developed by Morgan [50], which predicts an axisymmetric change of free-surface height due to a buoyant sphere of radius b rising through a viscous mantle. The model relates buoyant and viscous stresses to vertical deflection of the free surface [50,51]. To simplify our analysis, we choose a sphere depth $Z_d = b\sqrt{4/3}$ such that the topography takes the simple form shown in Figure 2c. In this case, the topographic profile is

$$h(x) = h_0 \frac{16b^5\left(8b^2 + 21x^2\right)}{\left(4b^2 + 3x^2\right)^{7/2}} \qquad \text{with} \quad h_0 \equiv \frac{3}{4}\frac{\delta\rho}{\rho_m} b, \tag{2.11}$$

where h_0 is the uplift at $x = 0$, ρ_m is the density of the uplifted material, and $\delta\rho$ is the density difference between the mantle and the spherical plume head. Figure 2c shows that LNB slopes are relatively large for distances $x \lesssim 2b$. We refer to this radial extent as the swell size.

With our choice of Z_d, we further assume that radial dykes are fully emplaced before the plume head reaches the base of the lithosphere and begins to spread laterally [52]. Axisymmetric spreading of the plume head diminishes the dynamic topography and results in an axisymmetric plateau [53].

Morgan [50] shows that incorporating a crustal layer with significantly higher viscosity has a negligible effect on the predicted dynamic topography. We further consider the case where the overlying crust is an elastic layer. For reasonable parameters, we show in supplementary material section S.2(a) that the impact on the dynamic uplift remains negligible. We also note that axisymmetric flexure creates tangential (hoop) stresses [54], which act normal to the walls of radial dikes. However, based on analysis in supplementary material section S.2(a), we find the hoop stress to be negligible.

(d) Boundary condition at the lateral tip

In the close vicinity of the lateral tip, referred to as the 'nose region', the assumption that the dyke's cross-section is in a two-dimensional elastic equilibrium is no longer valid [28]. To avoid solving a fully three-dimensional problem, we approximate the dynamics in this region using near-tip asymptotic solutions [36]. The accuracy of this approach is demonstrated by a comparison between our pseudo-3D solution and an independent, fully 3D numerical solution in supplementary material section S.3.

The nose region is defined by the narrow region of the dyke where force balance is dominated by pressure and fracture toughness. Under these conditions, linear elastic fracture mechanics (LEFM) provides the opening profile at a small distance $s = l - x$ behind the dyke tip,

$$\lim_{s\to 0} w \sim \frac{K'}{E'} s^{1/2} \qquad \text{and} \qquad \lim_{s\to 0} \frac{\partial w}{\partial s} = \frac{K'}{2E'} s^{-1/2}, \tag{2.12}$$

where $K' \equiv 8K_c/\left(2\pi\right)^{1/2}$. Using the half-height a of the leading cross-section (defined as the closest cross-section to l containing fluid), the volume of fluid V_{tip} in the tip region can be calculated as

$$V_{\text{tip}} = \int_{-a}^{a}\int_{0}^{S} w \,\mathrm{d}s\,\mathrm{d}z = \int_{-a}^{a} \frac{2E'^2}{3K'^2} w^3 \mathrm{d}z, \tag{2.13}$$

where the point $s = S$ is the distance from the lateral fracture tip to the leading cross-section.

With the assumption that the advance of the tip is limited by the rate of volume flux into the tip region, we can write

$$\frac{\mathrm{d}V_{\text{tip}}}{\mathrm{d}t} = Q(x = l - S). \tag{2.14}$$

We equate the rate of tip propagation $v(x = l)$ with $\mathrm{d}S/\mathrm{d}t|_{z=0}$. The numerical treatment of the tip region is subtle and is discussed in Section 2(f).iii.

(e) Solidification and the stopping criterion

Magma solidification occurs along the dyke walls, where diffusive heat loss into the relatively cold host rock drives inward growth of a solid layer, toward the centre of the dyke (Fig. 2d,e). This layer reduces the aperture of the the dyke, working against pressure-driven opening. If the closure rate exceeds the opening rate at a fracture tip, the tip cannot propagate further [28]. In this section we derive a criterion at which this stopping occurs.

(i) The speed of solid growth

The rate of solidification and layer growth decreases with time as the magnitude of the thermal gradient decreases. Consideration of the details of this Stefan problem leads to a solution relating total thickness of the solid layer w_s to the time δt since magma came into contact with the host rock,

$$w_s(x, z, t) = \alpha(\delta t)^{1/2} \tag{2.15}$$

The constant of proportionality $\alpha \equiv 4\lambda\sqrt{\kappa}$ is determined by the thermal diffusivity κ (assumed identical for rock and magma) and by λ, a dimensionless constant related to the rock and

magma temperatures, the specific heat capacity, and the latent heat of solidification (details in supplementary material section S.4(a)) [28,37]. We assume the magma injected into the system is at its liquidus temperature (in our simplified model of a one-component melt, this is also the solidus temperature). For dykes in Earth's crust, α is in the range of 10^{-5} to 10^{-3} m s$^{-1/2}$ [37]. The cross-sectional area of the solidified layer within the host rock is

$$A_s = \int_{-a}^{a} w_s \, \mathrm{d}z, \tag{2.16}$$

which is used in evaluating the total mass conservation (2.10). In supplementary material section S.5 we discuss the influence of the vertical distribution of the solid on the centreline pressure.

(ii) A stopping criterion from solidification

Bolchover & Lister [28] and Dontsov [37] show that a dyke tip cannot advance at speeds below a threshold value at which closure by solidification is faster than opening by propagation. We establish this criterion here, beginning by noting that the total dyke opening is the sum of the fluid and solidified widths $w = w_f + w_s$.

When the dyke tip propagates at a constant speed v, distance behind the tip s in the asymptotic expressions (2.12) can be replaced by $v\delta t$. Moreover, at the critical tip speed, $w = w_s$, the dyke tip is blocked by solidified magma such that fluid can no longer flow past this location. Then, using the derivative of (2.15) with respect to δt to eliminate $\partial w/\partial \delta t$ from (2.12), we obtain the critical speed

$$v_\mathrm{c} = \left(\frac{\alpha E'}{K'}\right)^2. \tag{2.17}$$

This is our stopping criterion: a dyke tip that slows to a speed v_c becomes blocked by solidification and hence attains a speed of zero. This criterion applies to propagation in the vertical ($\partial a/\partial t$) and lateral ($\mathrm{d}l/\mathrm{d}t$) directions.

(iii) Cross-sections vertically blocked by solid

Figure 2e shows a cross-section where the dyke tips are vertically blocked. This situation occurs when the rate of vertical tip propagation $\partial a/\partial t$ decreases until it is equal to v_c, at which point it drops discontinuously to zero. Once blocked, the tips cannot restart propagation. Solidification that occurs after the moment of blocking causes the fluid height a to decrease with time. As the fluid-filled region retreats toward the cross-section's centre, the upper and lower tips experience varying stress intensities that differ from the critical value K_c that governed propagation. Combining the LEFM tip asymptote (2.12) with the solidification rate (2.15) we find the tip height evolves according to

$$\frac{\partial a}{\partial t} = -\left(\frac{\alpha E'}{K_I'}\right)^2. \tag{2.18}$$

where $K_I' \equiv 8K_I/(2\pi)^{1/2}$. Here, K_I takes the stress intensity appropriate to the current geometry as the fluid height decreases, rather than being constrained to the critical value K_c. This allows us to compute the rate at which the tip height decreases throughout the retreat process. In the case where $K_I = K_c$ we recover $\partial a/\partial t = -v_\mathrm{c}$.

(f) Discretisation and numerical solution

The overall approach to obtain numerical solutions of the governing equations is discretisation in space and time, with finite-difference methods to approximate derivatives. We prescribe a uniformly spaced mesh with spacing of Δx and Δz in the x and z directions. Below we describe how an explicit time-stepping scheme with adaptive step size is used.

At each time-step, four primary tasks must be undertaken.

(i) *Updating cross-sectional area and total volume transport.* We obtain Q by combining (2.2), (2.6) and (2.8). Two inputs are required: the topographic gradient that is obtained from (2.11) and the dynamic pressure p_f that is adopted from the previous time step. We update A_s using (2.16), integrating the solid width w_s from the previous time-step. Then, having updated Q and A_s, (2.10) is used for an explicit time-step to update the fluid-filled cross-sectional area $A_f(x,t)$.

(ii) *Updating height, width and dynamic pressure.* For each grid node in x along the centreline, we update variables a, p_f and w_f associated with the vertical cross section. Which equations are used depends on the status of the tips of the cross section: blocked or unblocked, as in Fig. 2. We describe the unblocked case in 2(f).(i) and the blocked-tip case in 2(f).(ii), below.

(iii) *Updating the lateral tip position and dyke length.* At the lateral tip, the nose region is treated separately from the vertical cross-sections that comprise the main dyke body. Treatment of the nose exploits the tip asymptotics reviewed above. Our numerical update based on this theory is described below in 2(f).(iii).

(iv) *Determining the size of the next time-step.* The size Δt of the subsequent step is chosen based on the cross-section with the largest centreline flow speed. This limits fluid displacement over the step to an approximately prescribed distance, which promotes stability and accuracy of the integration. This approach to determining Δt is akin to satisfying a Courant–Friedrichs–Lewy condition.

These numerical steps require appropriate boundary conditions at both lateral ends of the domain. At the source ($x = 0$), we impose a Dirichlet condition with constant pressure p_0. At the dyke nose, we apply a Neumann condition on the pressure p that ensures zero flux across this moving boundary. To initialize the simulation,

- the dyke height is set to a^* (derived in supplementary material section S.4(b)).
- the initial lateral length l and corresponding element areas are determined using the nose boundary condition, based on the width of the element at $x = 0$ (Sec. 2(d)).

Once initialized, the evolution of the dyke is governed by the behaviour of its cross-sections, which can exist in one of two states: vertically propagating or vertically blocked. For each cross-section along the dyke's length, the governing equations and solution procedure differ depending on this state.

(i) Vertically propagating cross-section

For vertically propagating cross-sections, we solve for four unknowns (a, p_f, w_f, w_s) through a sequential solution procedure. The process begins by updating the solid width w_s using Eq. (2.15). We then simultaneously solve for the fluid pressure p_f and dyke half-height a. This solution requires matching three conditions: the known fluid area A_f from Eq. (2.10), the solid area A_s from Eq. (2.16), and the pressure–area relationship from Eq. (2.5). These equations are solved subject to the constraint that $K_I = K_c$ at the tip (Eq. (2.3)). Finally, with p_f and a determined, we compute the fluid width w_f by integrating the pressures over the cross-sectional height using Eq. (2.4).

(ii) Vertically blocked cross-section

A cross-section transitions from vertically propagating to blocked when its change in height $\partial a/\partial t$ drops below v_c. In this blocked regime, the solution procedure follows a modified sequence to account for the different conditions at the tip. The new fluid height a is first updated through the tip reduction equation (2.18), which accounts for solid closure. With this height established, we determine the fluid pressure p_f in (2.2) by matching the known cross-sectional fluid area A_f from the conservation equation (2.10) with the pressure–area relationship from (2.5), while accounting

for the solid area. Unlike the propagating case, the opening-mode stress intensity factor K_I at the tips can now take any value, potentially resulting in a cuspate fluid tip. This change is reflected in the update of $K_I' = 8K_I/(2\pi)^{1/2}$ in (2.18). The final step determines the fluid width using Eq. (2.4).

(iii) Nose region of the dyke

The nose region requires special treatment, distinct from the main dyke body, with its evolution governed by the opening profile of the leading cross-section. At each time step, we first compute the opening profile of the leading cross-section ($w_f(x = l - s, z, t)$). Using this profile and LEFM tip asymptotics in the lateral direction (equation (2.13)), we calculate the new tip volume V_{tip} and determine the change in tip volume from the previous time step. This volume change directly specifies the required flux into the nose region via equation (2.14). We directly impose the computed flux as a boundary condition for the leading cross-section. A zero-flux condition is maintained at the tip-line itself, ensuring mass conservation throughout the nose region. During the simulation, when the nose length exceeds Δx, it enters a new, empty element which becomes the new leading cross-section. At this transition, the current tip volume is converted into an area within this leading cross-section using $V_{\text{tip}}/\Delta x = A_f$.

3. Results

First, we define a reference set of model parameters. These serve as a basis to evaluate the physical dimensions of our results. Following this, analytical results are provided in section 3(b) for dyke growth near the source, where fracture toughness is negligible. Section 3(c) considers lateral dyke propagation driven by source pressure, without topographic uplift. This context is used to evaluate the importance of turbulence and solidification. Lastly, in section 3(d) we analyse the case of propagation driven by a gradient in gravitational potential energy associated with topographic uplift.

(a) Reference parameters

The reference values for model parameters shown in Table 1 are used to obtain results shown in all subsequent figures, except where otherwise specified.

Name	Parameter	Value	Unit
Source Pressure	p_0	5	MPa
Plane-strain stiffness	E'	40	GPa
Fracture Toughness	K_c	5	MPa·m$^{1/2}$
Dynamic viscosity	η	10	Pa·s
Solidification parameter	α	10^{-3}	m·s$^{-1/2}$
Gravitational acceleration	g	10	m·s^{-2}
Crustal density gradient	R	0.002	kg·m^{-4}
Fluid density	ρ_f	3000	kg·m^{-3}
Wall roughness	w_R	5	mm
Swell height	h_0	1	km
Plume head size	b	250	km

Table 1. Reference values for model parameters.

A few brief considerations provide physical intuition for the less conventional parameters in this table. Our value of α corresponds to growth of a solid crust on the dyke walls with a thickness of 1 cm after 100 seconds. This increases to 30 cm after one day of contact with the wall rock. The

value of R is a conservative estimate and corresponds to an increase in crustal density with depth by 2 (kg m^{-3})/km, resulting in a dyke half-height at the source of 31.6 km. This represents a dyke intruding into a thick cratonic crust. Larger values like those estimated for the Canadian shield (e.g., $R = 0.02$ kg m^{-4}) would reduce the dyke half-height to 10 km. Our reference parameters result in a dyke that is around 9 m thick at the source. Larger widths require either increasing R or decreasing the effective rock stiffness. As width is directly proportional to stiffness (Eq. 2.4), reducing this by a factor of four yields dykes 36 m wide. Using (2.11), our density difference between the plume head and ambient mantle is around $\delta\rho = 20$ kg m^{-3}; this buoyancy causes the domal uplift profile and falls within the range of density contrasts due to thermal expansion provided by Sleep [55, Eq. 10]. We obtain the magma viscosity value using the model by Giordano *et al.* [56] applied to the geochemistry of the MacKenzie dykes [12, sample RE3115]. The estimated melt viscosity varies from 5 to 22 Pa s for temperatures of 1200 to 1000°C. To avoid blockage, the fracture front must travel at a speed >6.3 m/s.

(b) The case of zero fracture toughness

Toughness K_c can be neglected in the vertical cross-section to the first order. Its contribution to w_f scales with $a^{-1/2}$, whereas the Rg term scales with a^2 [28]. Here we exploit this to obtain a first approximation of the near-source dyke geometry. The following analytical expressions define the cross-sectional dyke height, width and area for zero fracture toughness. The closed-form solutions of equations (2.2)–(2.5) in the absence of toughness are [28]

$$\begin{aligned} \hat{a} &= 2\left(\frac{p_f}{Rg}\right)^{1/2}, \\ \hat{w}_f(z) &= \frac{2Rg\left(\hat{a}^2 - z^2\right)^{3/2}}{3E'}, \\ \hat{A}_f &= 4\pi\frac{p_f^2}{E'Rg}. \end{aligned} \tag{3.1}$$

Here, variables with a hat denote that K_c has been neglected. The cross-sectional opening has the form shown in Figure 2d. In supplementary material section S.2(b), we investigate whether a free surface influences this cross-sectional form and demonstrate that the effect is negligible. When flow within the dyke is laminar, the 3D flux and average cross-sectional fluid velocity from equations (2.8)–(2.9) reduce to

$$\begin{aligned} \hat{Q} &= -\frac{\partial p}{\partial x}\frac{224\pi}{3}\frac{p_f^5}{E'^3(Rg)^2\eta'}, \\ \hat{v} &= -\frac{\partial p}{\partial x}\frac{56}{3}\frac{p_f^3}{E'^2Rg\eta'}. \end{aligned} \tag{3.2}$$

We use these variables below.

(c) Dykes without topographic uplift

In this section we consider numerical solutions and approximate analytical expressions for dykes driven by source pressure alone. The effects of solidification and turbulence on the final dyke length are quantified only by the numerics. We first present numerical results under two simplifying assumptions: (a) fluid flow remains laminar throughout propagation, and (b) solidification effects in the dyke cross-section—including solid growth and blocking of the vertical tips—are negligible. Under these assumptions, tip blocking due to solidification is only taken into account at the lateral tip to arrest the dyke. The validity of these assumptions will be discussed subsequently.

Figure 3. Comparison of laterally propagating dyke structure without and with domal uplift. The numerical solution is shown at the point where the leading tip ceases to propagate, not in its final solidified form. The model parameters are detailed in §3(a). Here the model is constrained to simulate laminar flow and specifies that vertical tip-blockage cannot occur. **Panel a** shows a dyke 3.1 hours after initiation with a constant source pressure, when the LNB is flat. Contours represent the fluid width (w_f). Note that the x and z scales are not equal. **Panel b** shows a dyke under equal conditions except that the LNB is deformed by domal topographic uplift. The dyke is shown 19.2 hours after it initiated. In this panel, the maximum LNB uplift h_0 is 1 km, and this is plotted here with a vertical exaggeration of $10\times$ to highlight its distortion. **Panel c** shows the lateral tip speeds of the dykes from the upper two panels. Propagation ceases when the lateral tip speed is equal to the critical value (v_c) of 6.3 m/s.

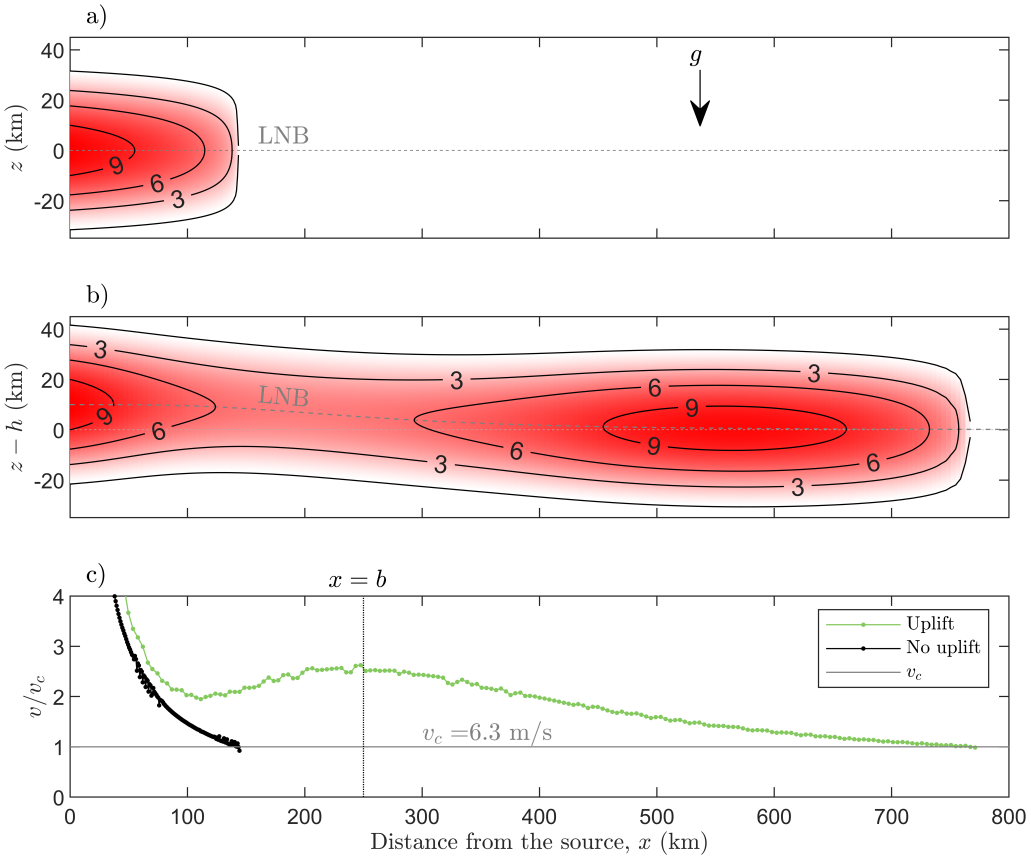

Figure 3a shows the results of our pseudo-3D numerical solutions using the reference parameters of Table 1 (with topographic uplift $h_0 = 0$). The dyke is driven by source pressure alone and is shown at the instant when the leading lateral tip becomes blocked ($v(x = l) = v_c$). The dyke is symmetric around the level of neutral buoyancy and its width decreases towards its lateral tip. Its largest width and height is at the source ($x = 0$). Here it is 10 m wide and 60 km tall; its final run-out length is 150 km. The tip speed as a function of distance is plotted in black on Figure 3c. It suggests power-law decay and, when plotted on log–log axes, the points follow a slope of -1, indicating an inverse scaling with distance. This scaling relationship obtained in numerical solutions will be derived by an approximate analysis below.

(i) Dyke length with constant source pressure

This section provides an analytical scaling for the length of a dyke driven by source pressure alone. Here we neglect fracture toughness, turbulence and cross-sectional solidification. This

Figure 4. Plots of dyke length (l) in the absence of uplift. **Panel a** shows the scaling of l with source pressure. Numerical results are presented for both laminar and turbulent flow conditions. The length $\hat{l}$ is from Eq. (3.5) and the numerical results are shown as dots and triangles. These simulations include fracture toughness and cross-sectional solidification. The half-height at the source a_0 is defined by (3.1). **Panel b** quantifies the effect of turbulence on the final dyke length. In this case, vertical tip blockage is prohibited. **Panel c** shows how including blockage of the vertical dyke tips influences the dyke length, with the flow constrained to be laminar. $\mathcal{S}$ from Eq. (3.8) provides an insight into the rate at which solidification slows the dyke to the point the lateral tip is blocked.

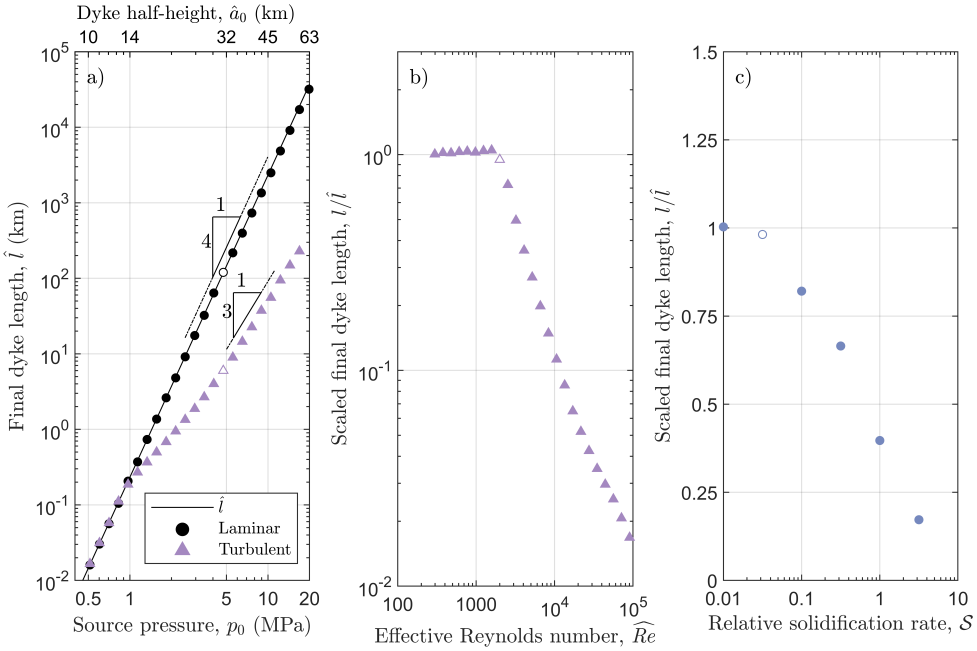

analytical scaling is used to discern the influence of these additional physics in sections that follow.

The fluid pressure in excess of lithostatic in the dyke is p_0 at its source, decreasing to zero at its leading tip ($x = l$). Thus the average pressure gradient must scale with the dyke length

$$\frac{\partial p}{\partial x} \approx \beta \frac{p_0}{l}, \tag{3.3}$$

where β is an unknown prefactor, to be determined, that accounts for 3D effects. Substituting this into (3.2) we find

$$\hat{v}^* = \beta \frac{p_0^4}{E'^2 R g \eta' l}, \tag{3.4}$$

which matches the $v \propto l^{-1}$ scaling we obtain from numerics. Using the numerics we obtain the prefactor as $\beta = 5.6$. Recalling that the critical velocity v_c defines the dyke length, substituting this and rearranging results in

$$\hat{l} = 5.6 \frac{K'^2}{\alpha^2 E'^4 R g \eta'} p_0^4. \tag{3.5}$$

This result is shown as a black line in Figure 4a. The source-pressure-to-length scaling is $\hat{l} \propto p_0^4$. This sensitivity causes the highest plotted pressure of 20 MPa to result in a dyke with a length approaching the Earth's circumference. Moveover, the height ($2\hat{a}$) of such a high-pressure dyke exceeds the typical thickness of Earth's crust—indicating that it would erupt.

Numerical results shown with markers in Figure 4a include the additional physics of fracture toughness and cross-sectional solidification. The close match with our scaling predictions shows that for reference parameters, these effects are of second-order importance.

Next we systematically quantify the effect that inclusions of turbulence, toughness and solidification have on final dyke length. We seek to determine whether these physical phenomena alter the scaling, making dykes less sensitive to source pressure.

(ii) The effect of turbulence on dyke length

To investigate how turbulence influences the final length $\hat{l}$, the same conditions as in the previous section are applied. We introduce the effect of turbulent flow using the empirical relationship described in section 2(b). Turbulence increases viscous dissipation and reduces the sensitivity of mean flow speed to changes in the driving pressure gradient, resulting in dykes that are shorter than those modelled in the preceding section, where laminar flow was explicitly assumed.

Purple dots in Fig. 4a shows the resulting dyke lengths when turbulence is included. As the source pressure increases, so does the dyke width and the fluid velocity. This results in higher Reynolds numbers, resulting in a transition to turbulent flow at a source pressure of around 1 MPa. This slows the lateral dyke speed relative to the laminar case, and reduces the final dyke length. Visual inspection of Figure 4a reveals that turbulence results in a scaling of approximately $l \propto p_0^3$. The dyke-length sensitivity to source pressure is thus decreased moderately by turbulence.

To better quantify this, we derive an effective Reynolds number for dykes driven by source pressure alone. Substituting the zero-toughness expressions from Sec. 3(b) into Equation (2.7), where $q \approx w_f v$ and $\hat{w}_f = \hat{A}_f/(2\hat{a})$, and using our estimate of the mean laminar flow speed at the source $\hat{v}$, when the dyke is length $\hat{l}$ from equation (3.5), we find

$$\widehat{Re} = 24\pi \frac{E'\alpha^2 p_0^{3/2} \rho_f}{K'^2 R g^{1/2} \eta'}. \tag{3.6}$$

The effective Reynolds number allows us to predict whether turbulence will influence the final dyke length. This Reynolds number is evaluated at the characteristic length that would be achieved under purely laminar flow conditions. Fig. 4b shows that when $\widehat{Re}$ exceeds approximately 2000, turbulence becomes significant and reduces the dyke length relative to the laminar prediction $\hat{l}$. This occurs because turbulent flow has increased viscous dissipation, causing the dyke to terminate at a shorter length than predicted under laminar flow. For our reference parameters (shown as a open circle), the length is around twenty times shorter due to turbulence. Thus turbulence means dykes require higher pressures to propagate similar distances. Such pressures will increase the dyke's vertical extent, making dykes with high $\widehat{Re}$ prone to eruption before significant lateral propagation occurs.

The empirical turbulence relation in Section 2(b) requires a measure of the wall roughness. However, we show in supplementary material section S.1(d) that varying wall roughness in a reasonable range around our reference value does not significantly affect the turbulence because megadykes are wide relative to the roughness scale.

In the following sections, turbulence is neglected. This allows us to more clearly quantify the influence of other physical effects. A discussion of turbulence in the context of dykes with domal uplift is provided in supplementary material section S.4(c). For turbulent dykes in the presence of domal uplift, we observe similar trends in relation to their laminar counterparts. Similar pressure–length scaling and then a transition to topographic dominated lengths occurs, but at systematically higher source pressures to achieve equivalent dyke lengths.

(iii) The effect of solidification dynamics on the cross-sectional form of the dyke

Until now, tip blocking due to solidification has been taken into account at the lateral tip, but has been neglected at the vertical tips. Here we explore the influence of solidification on the cross-sectional dyke form, to understand if its inclusion is warranted or we can neglect this in the case of mega-dykes. Solidification may block the upper and lower dyke tips, stopping them from propagating to their full vertical extent (Fig. 2d, e). Thus the dyke profile will be less vertically extensive than shown in Fig. 3. In addition to tip-blocking (§2(e).(iii)), the growth of solid removes fluid from the system. Figure S7 in supplementary material section S.6 shows a

comparable simulation but where solidification is included. In the two cases without uplift, the dyke widths are similar but the height is reduced by ∼10 km. Hence the model indicates that tip blocking can limit the vertical extent of a dyke, thereby reducing the propensity for eruption at the surface [15].

While Bolchover & Lister [28] account for solidification effects, they do not directly compare models with and without solidification of the vertical tips, making it difficult to isolate this influence on overall dyke length. Although vertical-tip blockage is physically reasonable—particularly in a model where lateral-tip blockage provides our main result (dyke length)—we test whether capturing it significantly impacts our results, or if it can be neglected at leading order. We approach this by deriving a dimensionless parameter to characterize how vertical tip-line solidification affects the scaled dyke length compared to a calculation that neglects this.

We begin by characterizing solidification through a velocity scale, v_s^*, which gives an indication of the rate at which the solid grows inwards, in the y direction,

$$v_s^* = \frac{p_0^{1/2}\alpha}{\eta'^{1/2}}. \tag{3.7}$$

By comparing this to the critical propagation speed v_c, which acts in the x and z directions, we define a dimensionless ratio of velocities,

$$\mathcal{S} = \frac{v_s^*}{v_c} = \frac{K'^2 p_0^{1/2}}{E'^2 \alpha \eta'^{1/2}}. \tag{3.8}$$

Figure 4c shows that increasing $\mathcal{S}$ reduces the scaled dyke length. Notably, α appears in the denominator of this expression, highlighting a counter-intuitive relationship: higher values of α (faster solidification) actually produce lower values of $\mathcal{S}$, and thus corresponds to dykes where solidification has less influence on the final, scaled length. This occurs because higher solidification rates cause earlier lateral blockage. The resultant shorter propagation distance means reduced contact time with wall rock, which actually decreases the opportunity for vertical tip blockage to fully develop—despite the increased solidification rate. This means that the form of the dyke when it terminates, shown in Fig. S7a will tend towards the more elliptical tip-line shape shown in Fig. 3, as α is increased, whilst its final length would decrease.

Overall, these results indicate that variations in α have a minimal impact on the final dyke length. Our reference parameter for α is a high-end estimate, representing the fastest possible solidification rate under typical crustal and magmatic conditions, based on Dontsov [37]. For the properties described in Sec. 3(a), $\mathcal{S}$ is calculated to be 3×10^{-2}. Therefore, it appears that when solidification causes vertical-tip blocking, reducing the dyke height, this reduction in height does not significantly influence the location where the lateral tip arrests. This reduction in vertical-tip height also has minimal influence on the width variation along the dyke for reasonable properties. We have therefore excluded solidification of the vertical-tip line from models in the forthcoming sections, facilitating the derivation of scaling laws.

(d) Dykes driven by domal topographic uplift

In this section, we examine how domal uplift associated with a rising plume head (§2(c)) influences final dyke length. Figure 3b shows a dyke profile where domal uplift has warped the level of neutral buoyancy. This dyke propagates five times further than a dyke under identical conditions except without uplift (Fig. 3a). The dyke with uplift is symmetric in z around the LNB. It is initially wide and tall but narrows and shortens as the LNB slope increases. Where the slope is highest ($x \approx b$), the dyke's centreline width has halved. The width increases again where the LNB flattens. In these areas of shallow topography, the fluid begins to accumulate due to reduced driving force and flow speed; this eventually causes the lateral tip to arrest. The final dyke length is approximately three times the plume head radius b. Panel c shows the dyke-tip speed follows a related pattern, rapidly decreasing in its initial stages as the dyke lengthens and the gradient due to the source pressure drops, speeding up again where the LNB slope is largest ($x \approx b$), and then

slowly decaying beyond this. In the following sections we investigate this behaviour in greater detail, excluding turbulence and solidification (we consider these effects further in supplementary material section S.4(c)).

(i) The effect of uplift size and shape on dyke length

Figure 5 explores the effect of properties of the domal uplift on the final dyke length. In each panel, a single parameter is varied away from its reference value, while all others are held constant. Broadly, these calculations show that when the topography is high enough to influence dyke speed, dykes can propagate hundreds to thousands of kilometres. In panel a, we see that for topographic swells with small height h_0, dynamic topography has a negligible effect on the final dyke length. In these cases, the gravitational potential energy by the uplift is insignificant relative to the pressure gradient arising from the source pressure. Therefore, the length of these dykes tends towards $\hat{l}$, the length of a dyke without uplift.

To explore how the height profile of the swell (2.11) influences dyke length, we examine the average slope of the LNB between the dyke source and the effective radius of the swell. The steepest part of the topography—at the inflection point—is close to b and thus, for the sake of convenience, we define the swell's characteristic size as $2b$. This represents the distance over which the topographic effect is significant; at further distances the uplift is negligible. We hence estimate the average slope as $h_0/(2b)$, where h_0 is the maximum uplift at the source. This results in an equivalent pressure gradient between $x = 0$ and $2b$ of approximately $\rho_f g\,(h_0)\,/\,(2b)$. This indicates that increased central uplift (h_0) and smaller head-sizes (b) will result in faster and longer dykes.

When we account for the hotspot topography, our numerical results confirm these trends. Figure 5a shows how increasing h_0 significantly increases the final dyke length. There is a transitional value of h_0 at 250 m at which there is a marked increase in the final dyke length. Above this, the dyke lengths exceed the swell size. In contrast, Fig. 5b shows when the plume head size is increased, the dyke length decreases. This effect saturates for head sizes in the range of 200 to 400 km. The dyke length then rapidly decreases towards the length $\hat{l}$, determined by the source pressure.

Figure 5c shows how the dyke length depends on the source pressure. Low pressures have pressure-dominated dyke lengths. A step is observed as the pressure is increased, resulting in dykes propagating further than the swell size b. This occurs when the pressure-driven dyke length becomes great enough to extend beyond the initial flat portion of the swell and into the region where the increasing topographic slope takes over as driver of the flow, accelerating the leading tip (Fig 3c). After this transition, dyke length still follows a scaling akin to the $l \propto p_0^4$ scaling. Then, at higher source pressures, we find from fitting our numerics that a $l \propto p_0^{11.5}$ power law scaling occurs.

Each panel of figure 5 shows the dyke length predicted using a reduced set of physics represented as an ordinary differential equation (ODE; dashed line), derived in supplementary material section S.7 (Eq. (S13)). This prediction matches well with the numerical predictions of the dyke length. Note that the ODE does not account for the dyke's head region, resulting in shorter dykes than the numerical model. The reduced physics in our ODE model follows from observations of our numerics showing that the 3D flux quickly stabilizes during dyke propagation when there is a slope, allowing us to simplify the system into an equation describing tail shape and fluid flow. We neglect solidification effects and the dyke's head-region dynamics, while approximating weight gradients and assuming a stable dyke profile after the tip passes. This simplified approach captures the essential pressure dynamics governing dyke propagation over domal uplift.

We use the solutions of the ODE to answer the following questions:

(i) How does the dyke shape vary over the swell and which parameters define this?
(ii) What conditions are required for the dyke length to exceed the size of the plume head b?

Figure 5. Plots of dyke length l in the presence of domal uplift, showing how uplift parameters affect the final dyke length. The default parameters from Table 1 are held constant whilst the influence of one control parameter is investigated. Here the flow is constrained to be laminar and we disregard vertical tip blockage and solid growth. **Panel a** shows how the peak uplift (h_0) at $x = 0$ influences the dyke length. The y axis is length relative to the analytical prediction $\hat{l}$ for no uplift. **Panel b** shows the dyke length as a function of the plume-head size with the same y axis as panel a. **Panel c** shows the influence of the source pressure, with lengths scaled relative to the hotspot size.

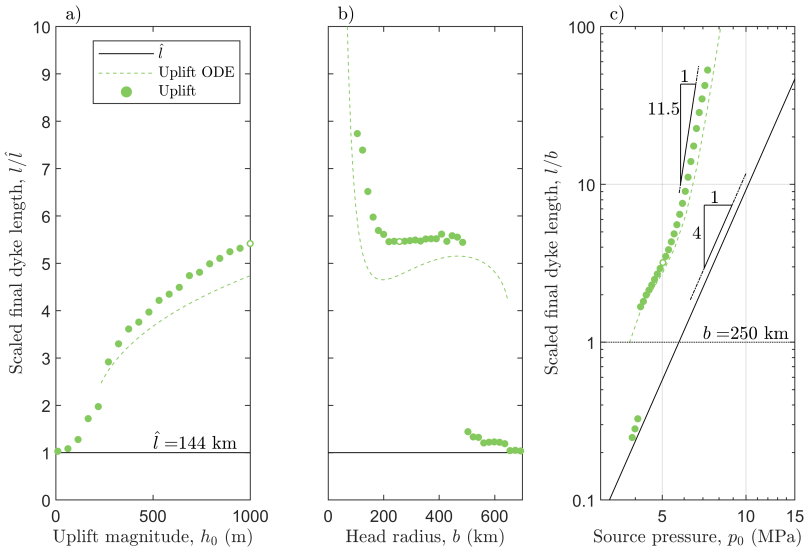

In the next section, we use the ODE to estimate the dyke shape and the position of the transition from pressure-dominated to topography-dominated length. We show this is controlled by a single non-dimensional number. This dimensionless parameter—a pressure ratio—defines the dyke opening and shape, as shown in Fig. 6b,c.

(ii) A predictor of dyke length in the presence of domal uplift

Here we study the non-dimensionalised ODE model (Eq. (S13)) derived in supplementary material section S.7. This simplified equation, motivated by numerical solutions, reveals the parameters that have leading-order control on the dyke shape.

The ODE models the dyke pressure along its length, leading to an understanding of its cross-sectional shape and fluid velocity. A non-dimensional ratio of pressure scales arises from the ODE model, $\mathcal{P}$, defined as

$$\mathcal{P} = D\left(\frac{p_0}{h_0 \rho_f g}\right)^{23/20}, \tag{3.9}$$

where D is around 2.6 and is defined in (S12). $\mathcal{P}$ is the ratio of the source pressure relative to the gravitational potential term. The gravitational potential term, $h_0\rho_f g$, represents the hydrostatic pressure difference between the source origin $x = 0$ and the far-field $x = \infty$ where the topographic uplift vanishes. This ratio effectively compares the source pressure to the potential pressure drop along the dyke's length, controlling whether propagation is dominated by the driving pressure at the source or driven by the topographic gradient along the dyke path. Fig. 6 demonstrates how this model answers our two questions above. The figure shows that $\mathcal{P}$ controls the dyke's shape in our non-dimensional scaling.

Addressing our first question, Fig. 6b shows how dyke shape varies over the swell. The key finding is that dyke height follows a characteristic pattern: half-height first decreases where the

topography is steepest (around $x \approx b$) and then increases with distance from the source as the topography flattens. This creates a "pinched" dyke profile over the steepest part of the swell, followed by expansion in the far field. The figure demonstrates that the magnitude of this shape variation is controlled by the parameter $\mathcal{P}$—lower values (topography-dominated conditions) produce more pronounced shape changes, while higher values (pressure-dominated conditions) result in more uniform dyke shape.

The physical mechanism behind this shape variation is volume conservation. Our numerical results show that the source flux stabilizes as the dyke lengthens over the topography. To maintain constant flux through each cross-section, the dyke must narrow (reducing both height and width) where fluid flow is fastest—specifically near the steepest point of the topography where the pressure gradient is greatest. Notably, the location of this minimum cross-section is rather insensitive to $\mathcal{P}$, occurring consistently near the inflection point of the topography. After the topography flattens, reduced topographic gradients allow dykes to expand again, becoming taller than at their source.

Regarding our second question about conditions for dyke length to surpass b, the velocities plotted in Fig. 6c provide insight. The figure shows that when $\mathcal{P}$ is low (topography-dominated regime), dykes maintain higher velocities over much greater distances compared to high-$\mathcal{P}$ cases (pressure-dominated regime). This extended high-velocity region directly translates to longer dyke propagation distances. Note that we have scaled the resulting dyke velocity by equation (S7), the mean flow speed at the source, which is derived in supplementary material section S.7. If the critical velocity is close to the source velocity then topography-dominated dykes will extend well beyond the plume head size b, while pressure-dominated dykes remain confined to distances comparable to $2b$.

4. Discussion

We investigated the hypothesis that the topographic uplift above a buoyant mantle plume is a key control on the mean length of radial dyke swarms. Our simulations support this hypothesis, demonstrating that dynamic topography provides the primary mechanism for generating the observed characteristic lengths of megadykes. The topographic effect remains robust regardless of assumptions about fluid flow, solidification processes, or crustal properties. In this section, we address the key questions raised in our introduction.

(a) Reconciling high source pressure with lateral rather than vertical propagation

We asked: if a large source pressure is required to overcome viscous drag and drive dykes great distances, why does this same overpressure not drive magma upward through the free surface instead? Our modelling provides a clear answer. In the absence of topographic uplift, dykes driven solely by source over-pressure require relatively high source pressures to achieve significant propagation distances. At these pressures, vertical confinement due to density and/or solidification is not enough to prevent the vertical extent of the dykes from becoming unrealistically large, predicting eruption near the magma source. This contradicts observations of megadykes that propagate laterally for hundreds of kilometres without erupting and indicated that source pressure alone cannot explain megadykes.

When accounting for domal uplift above a plume head, we find that dykes can propagate hundreds of kilometres at source pressures lower than 5 MPa. This critical insight explains how megadykes can achieve observed run-out lengths without triggering vertical eruption near the source. The potential-energy gradient created by topographic uplift efficiently drives lateral propagation while minimizing vertical extension, reducing the likelihood of near-source eruption.

Megadykes are prevented from erupting by two mechanisms: (1) confinement at levels of neutral buoyancy where the density of the crust matches that of the magma, and (2) vertical-tip

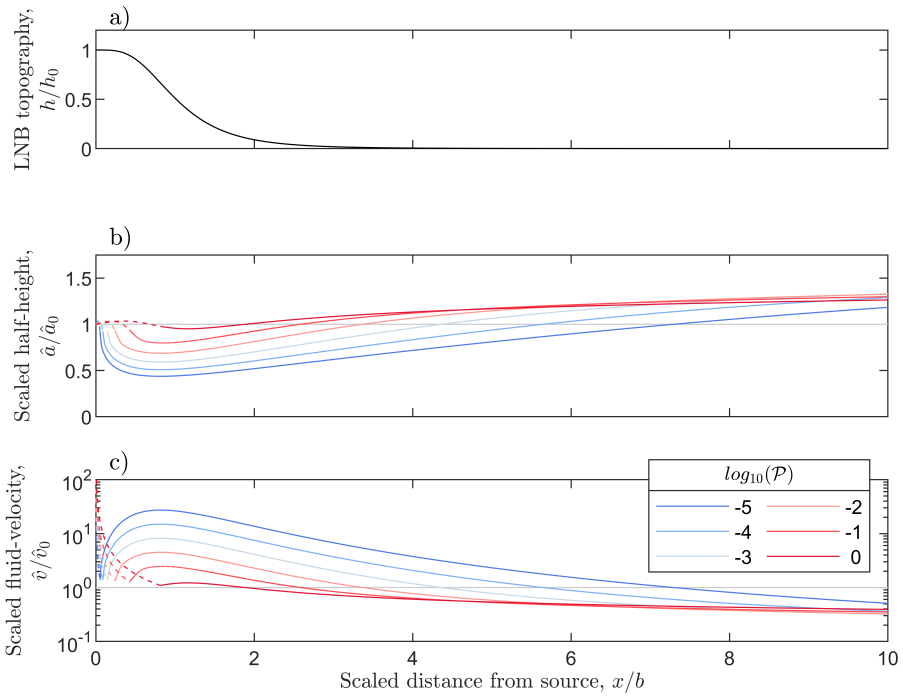

Figure 6. Dyke half-height and flow speed in the presence of domal uplift for different values of the non-dimensional pressure $\mathcal{P}$ (3.9). Low $\mathcal{P}$ values represent dykes dominated by topographic stress gradients and high-$\mathcal{P}$ dykes are dominated by source pressure. The results here are obtained using the ODE model (Eq. (S13)). **Panel a** Topographic LNB profile; **Panel b** Dyke half-height (3.1); **Panel c** Fluid velocity at a given distance from the source, scaled by the flow speed at the source once the flux has stabilised (S7). In Figure 3 we see that even in the presence of topography, the front speed initially decays in the same manner as a dyke propagating without topography; the dashed lines show our analytical approximation (3.4) for front speeds from the pressure-driven regime without topography.

blockage due to solidification. The neutral buoyancy level creates the primary physical barrier to vertical propagation, as pressure that drives magma upwards is counteracted by negative buoyancy forces. Simultaneously, solidification at the vertical tip can block upward propagation when the vertical propagation of the tip is sufficiently slow.

In the presence of domal uplift, dyke heights increase as the surface slope flattens, which typically occurs at distances approaching and exceeding the plume-head radius. This increases their propensity for eruption in distal regions, explaining observations of some dykes breaching the surface and/or erupting near their terminus. As we demonstrate in supplementary material section S.2(b), dykes perched at their level of neutral buoyancy that breach the ground surface can maintain mechanical stability and retain most of their magma content below the surface, rather than undergoing complete evacuation upon breaching the surface. This mechanism explains the often-limited nature of volcanism from large dykes from small shields and flows.

(b) Controls on dyke termination distance

Our second question asked what determines where laterally propagating dykes ultimately stop. Based on observations that source volumes do not limit dyke size in general, we adopted a constant-pressure boundary condition and identified solidification at the dyke tip as the primary termination mechanism.

Our analysis reveals that for dykes propagating in the presence of domal uplift, the final length is controlled by the interaction between the topographic gradient and solidification processes at the leading tip. Tip blockage occurs when propagation speed falls below a critical threshold where solidification outpaces the opening rate. For dykes driven by sustained source pressure in the presence of domal uplift, this speed threshold is typically reached at distances comparable to (or slightly greater than) twice the underlying plume-head radius, as the flattening topographic gradient causes deceleration of the leading tip. This creates a characteristic length scale for dykes within a swarm that is related to the underlying plume dimensions.

(c) Explaining uniform dyke lengths within swarms

Our third question asked why do the majority of megadykes in a given swarm exhibit similar lengths. This uniformity is challenging to explain with models that depend solely on source pressure, given the extreme sensitivity of length to pressure that we identified. Our topographic-control model provides a straightforward physical explanation for this observation.

In the presence of domal uplift, low source pressures are sufficient to drive dykes laterally to distances matching the scale of the topographic swell. Assuming dyke propagation begins once a critical source-pressure threshold is crossed, excess pressures significantly above this threshold are unlikely to be sustained, as dyke initiation would occur as soon as the critical pressure is reached.

This mechanism creates a natural length scale for dykes within a swarm that is directly tied to plume-head dimensions. The occasional outlier dykes that extend 2–3 times beyond the norm require only marginally higher source pressures that remain within a realistic range, given the sensitive pressure–length scaling we have identified.

(d) Effects of turbulent flow on megadyke propagation

Our fourth question was whether flow in megadykes is turbulent and, if so, what effect this would have on run-out length. Our model predicts when turbulence occurs without uplift, and shows that it changes the pressure-to-length scaling from $l \propto p_0^4$ to $l \propto p_0^3$. In this system, we show that the onset of turbulence is most sensitive to the solidification parameter α and the fracture toughness K_c.

When flow becomes turbulent, higher pressures are required for extensive lateral propagation due to increased energy dissipation. Turbulent flow reduces the sensitivity of flow speed to changes in the driving pressure gradient. Without topographic uplift, the higher pressures required for extensive lateral dykes make these more likely to erupt near their source. However, in the presence of topographic uplift, even turbulent flow can be sustained with moderate source pressures, enabling lateral propagation on the length scale of the swell size, without near-source eruption.

Importantly, while turbulence modifies the quantitative relationship between source pressure and dyke length, it does not change our fundamental conclusion that topographic uplift is the primary control on megadyke propagation distances. This demonstrates that the topographic effect is robust to variations in flow regime, providing further evidence for our central hypothesis.

(e) Limitations and observational constraints

Our results emerge from a theoretical framework that necessarily makes simplifying assumptions. We assume a spatially uniform crust in terms of density, toughness, and stiffness. This appears reasonable for regions like the Canadian shield based on seismic velocities, but may not hold in all geological settings. Observations on Earth and other planetary bodies show little correlation between megadyke geometry and crustal structure, indicating that the LNB, rather than layering of the host rock, provides the primary vertical constraint [57,58]. We also neglect both regional

tectonic stresses and dyke interaction, both of which have been shown to influence megadyke pathways and their spacing [18,19,59].

Our model assumes magma injection at its liquidus temperature. Lister [34] demonstrates that for a dyke propagating downslope, in a laminar flow regime, fed by a constant flux of superheated magma, the nose remains at the liquidus temperature except at early times. This is consistent with our use of a solidification-based stopping criterion. Furthermore, applying our reference parameters for reasonable thermal properties shows that even extreme superheat of the fluid produces negligible meltback of the dyke walls (orders of magnitude smaller than dyke width) on arrest timescales. Thus, the liquidus-injection assumption does not affect our results [34]. Dyke width can increase by processes that are not included in our model such as anelastic deformation, melting and erosion.

Three key parameters in our model are poorly constrained and may vary by orders of magnitude in natural systems: magma viscosity, fracture toughness, and the solidification factor α. Significantly, our sensitivity analysis shows that these variables influence our length scaling $\hat{l}$ less strongly than source pressure and host-rock stiffness. This relative insensitivity to the most uncertain parameters strengthens confidence in our primary conclusions despite these uncertainties.

We employ a constant-source-pressure boundary condition and neglect magma compressibility, which simplifies the analysis while capturing the essential physics. Models that couple magma chambers and dykes would introduce additional parameters and geometric factors but could provide time-dependent evolution of pressure. However, our constant-pressure approach is justified by observations that megadyke propagation is typically not limited by magma supply, as discussed earlier.

Observations of dyke swarms are inherently limited to those that are detectable, either through surface expressions (grabens on Venus) or geophysical methods (aeromagnetic surveys on Earth) [6,14]. Data indicates that the angular dyke spacing is smaller closer to the magma source, suggesting a greater angular density of dykes near the source in these swarms [19]. This raises the possibility of an observational bias, as only those dykes that are close enough to the surface and propagate sufficiently far are typically included in defining the radial extent of each swarm. Our model primarily addresses these detectable dykes, which may represent only a subset of the total dyke population.

Despite these limitations, the robustness of our central finding—that topography provides the dominant control on dyke propagation—suggests that our conclusions would hold even with more complex model assumptions.

5. Conclusions and further work

This work presents novel 3D models of laterally propagating dykes and quantifies the controls on their final lengths. Our modelling integrates four key physical processes that have not previously been combined in pseudo-3D dyke models: source pressure, turbulent flow, solidification, and the potential energy of domal uplift. The integration of these processes creates a framework that resolves long-standing questions about megadyke formation and propagation.

Our results robustly support the hypothesis that dynamic topography above a buoyant mantle plume is the primary control on megadyke propagation distances. Our modelling demonstrates that this topographic mechanism explains why megadykes can propagate great distances without near-source eruption: the topographic gradient enables lateral propagation at lower source pressures ($\sim$5 MPa) than would be required in its absence.

Our key finding is that the average lengths of dykes in radial swarms are directly related to the size of the underlying plume head, typically extending to approximately two times the plume-head radius. The extreme pressure sensitivity we identify explains how occasional outliers that extend much farther than the typical swarm length can occur in systems modulated by a critical pressure threshold. This represents a significant advance over previous models that struggled to explain these observations simultaneously.

The identification of dynamic topography as the primary control on megadyke propagation has implications for interpreting the geological record of plume–lithosphere interaction. In particular, our model provides a direct link between observable dyke lengths and the size of ancient plume heads, offering a new tool for reconstructing mantle dynamics through Earth's history. The characteristic length scale imprinted on radial dyke swarms serves as a fingerprint of the underlying plume, while variations in dyke lengths contain information about source pressure conditions during emplacement. Several aspects of megadyke formation warrant further investigation.

(i) Observational tests. Our model provides several testable predictions for field and remote-sensing studies. For dykes driven by topographic gradient, we predict a distinctive, non-monotonic pattern in dyke profile: dyke width and height should decrease with distance from the source until approximately the plume-head radius (b), where the LNB topography was steepest, then increase again beyond this distance. This change should also be evidenced in the changing depth and throw of overlying graben systems that grow due to the dyke-induced stresses [16]. We also predict that outlier dykes within each array that extend significantly farther than the average will consistently display greater width and height.

(ii) Tip dynamics. Observations of natural and experimental fluid-filled fractures reveal complex start–stop behaviour during propagation [38–40]. Our model employs a simplified solidification criterion that reasonably approximates the time-averaged behaviour of dykes, but does not fully capture this unsteady propagation regime. The interaction between tip dynamics and solidification processes warrants further investigation to better understand arrest mechanisms. Such studies would help assess how well time-averaged models represent episodic dyke behaviour.

(iii) Late-stage evolution. After the leading tip becomes blocked, continued lateral flow may widen the distal end of the dyke. Understanding this process would provide additional constraints for interpreting field observations of solidified dykes.

(iv) Circumferential dyke swarms. These distinctive swarms are frequently associated with giant radial swarms on Earth [60], but follow fundamentally different propagation patterns. While the radius of circumferential swarms is generally thought to be controlled by the mechanics of plume-head spreading, our model for radial dykes suggests that both types may encode complementary information about evolving plume dimensions. A comprehensive analysis comparing the conditions required for the formation and propagation of circumferential dykes with their radial counterparts could provide a more complete picture of plume–lithosphere interaction. By integrating observations of both swarm types, we may develop a more robust framework for reconstructing ancient plume dynamics. This may enable more accurate constraints on parameters such as plume-head size, spreading rates, and topographic evolution.

Dynamic topographic uplift above mantle plumes provides the key mechanism for explaining the enigmatic properties of megadyke swarms. By enabling lateral propagation at moderate source pressures, topography creates the conditions necessary for the development of the extraordinary dyke lengths observed in these systems while simultaneously explaining their resistance to near-source eruption. The characteristic length scale imposed by the plume-head size becomes imprinted on the resulting dyke swarm, as it controls when these decelerate and arrest, creating a geological fingerprint of past mantle dynamics. This work advances understanding of how mantle plumes interact with the lithosphere to create these remarkable magmatic features observed on planetary bodies throughout the Solar System, offering new insights for interpreting plume activity and constraining convective processes in planetary interiors.

Acknowledgements. This research received funding from the European Research Council under Horizon 2020 research and innovation program grant agreement number 772255 and 101003173. AEP is funded by the Royal Society (URF\R1\231613). We thank J. Cartwright, R. Ernst and P. England for insightful discussions

and feedback on the model, A. Möri and B. Lecampion for promptly addressing questions related to PyFrac, J. Kavangh, O. Melnik, and J. Birnbaum for their inquiries about turbulent flow. We thank the three reviewers for their constructive feedback and detailed comments.

References

1. Ernst RE, Head JW, Parfitt E, Grosfils E, Wilson L. 1995 Giant radiating dyke swarms on Earth and Venus. *Earth-Science Reviews* **39**, 1–58. (10.1016/0012-8252(95)00017-5)
2. Ernst RE. 2014 *Large igneous provinces*. Cambridge University Press.
3. El Bilali H, Ernst RE. 2024 Far-travelled 3700 km lateral magma propagation just below the surface of Venus. *Nature Communications* **15**, 1759. (10.1038/s41467-024-45603-6)
4. Ernst RE, Desnoyers D, Head J, Grosfils E. 2003 Graben–fissure systems in Guinevere Planitia and Beta Regio (264–312 E, 24–60 N), Venus, and implications for regional stratigraphy and mantle plumes. *Icarus* **164**, 282–316. (10.1016/S0019-1035(03)00126-X)
5. Studd D, Ernst R, Samson C. 2011 Radiating graben–fissure systems in the Ulfrun Regio area, Venus. *Icarus* **215**, 279–291. (10.1016/j.icarus.2011.06.026)
6. Fahrig W, Jones D. 1969 Paleomagnetic evidence for the extent of Mackenzie igneous events. *Canadian Journal of Earth Sciences* **6**, 679–688. (10.1139/e69-065)
7. Fahrig WF, West TD. 1986 Diabase dyke swarms of the Canadian Shield, Map 1627A. *Geological Survey of Canada*. (10.4095/133917)
8. Halls H. 1982 The importance and potential of mafic dyke swarms in studies of geodynamic processes. *Geoscience Canada* **9**, 145–154.
9. Halls H, Fahrig W. 1987 Dyke swarms and continental rifting: some concluding remarks. *Mafic Dyke Swarms. Geological Association of Canada, Special Paper* **34**, 483–492.
10. Parker A, Rickwood P, Tucker D. 1990 Mafic Dykes and Emplacement. In *Proceedings of the Second International Dyke Conference Adelaide, South Australia* pp. 12–16.
11. Ernst RE, Baragar W. 1992 Evidence from magnetic fabric for the flow pattern of magma in the Mackenzie giant radiating dyke swarm. *Nature* **356**, 511–513. (10.1038/356511a0)
12. Baragar W, Ernst R, Hulbert L, Peterson T. 1996 Longitudinal petrochemical variation in the Mackenzie dyke swarm, Northwestern Canadian Shield. *Journal of Petrology* **37**, 317–359. (10.1093/petrology/37.2.317)
13. Koenig E, Pollard DD. 1998 Mapping and modeling of radial fracture patterns on Venus. *Journal of Geophysical Research: Solid Earth* **103**, 15183–15202. (10.1029/98JB00577)
14. Parfitt E, Head J. 1993 Buffered and unbuffered dike emplacement on Earth and Venus: implications for magma reservoir size, depth, and rate of magma replenishment. *Earth, Moon, and Planets* **61**, 249–281. (10.1007/BF00572247)
15. Carver F, Cartwright J, McGrandle A, Kirkham C, Pryce E. 2023 The continuation of the Mull Dyke Swarm into the Southern North Sea. *Journal of the Geological Society* **180**, jgs2023–039. (10.1144/jgs2023-039)
16. Rubin AM, Pollard DD. 1988 Dike-induced faulting in rift zones of Iceland and Afar. *Geology* **16**, 413–417. (10.1130/0091-7613(1988)016%3C0413:DIFIRZ%3E2.3.CO;2)
17. Hou G. 2012 Mechanism for three types of mafic dyke swarms. *Geoscience Frontiers* **3**, 217–223. (10.1016/j.gsf.2011.10.003)
18. Blackstone LA, Grossman-Ponemon BE, Heimisson ER, Lew AJ, Segall P. 2024 Modeling dike trajectories in a biaxial stress field with coupled magma flow, fracture, and elasticity. *Bulletin of Volcanology* **86**, 52. (10.1007/s00445-024-01734-8)
19. Bunger AP, Menand T, Cruden A, Zhang X, Halls H. 2013 Analytical predictions for a natural spacing within dyke swarms. *Earth and Planetary Science Letters* **375**, 270–279. (10.1016/j.epsl.2013.05.044)
20. Pinel V, Jaupart C. 2004 Magma storage and horizontal dyke injection beneath a volcanic edifice. *Earth and Planetary Science Letters* **221**, 245–262. (10.1016/S0012-821X(04)00076-7)
21. Möri A, Garagash D, Lecampion B. 2023 Transition from Vertical to Lateral Diking at the Neutral Buoyancy Line. In *European Geosciences Union, Annual Meeting 2023 (EGU2023)*. (10.5194/egusphere-egu23-15623)
22. Lister JR. 1991 Steady solutions for feeder dykes in a density-stratified lithosphere. *Earth and Planetary Science Letters* **107**, 233–242. (10.1016/0012-821X(91)90073-Q)
23. Pollard DD, Townsend MR. 2018 Fluid-filled fractures in Earth's lithosphere: gravitational loading, interpenetration, and stable height of dikes and veins. *Journal of Structural Geology* **109**, 38–54. (10.1016/j.jsg.2017.11.007)

24. McKenzie D, McKenzie JM, Saunders RS. 1992 Dike emplacement on Venus and on Earth. *Journal of Geophysical Research: Planets* **97**, 15977–15990. (10.1029/92JE01559)
25. Fialko YA, Rubin AM. 1999 Thermal and mechanical aspects of magma emplacement in giant dike swarms. *Journal of Geophysical Research: Solid Earth* **104**, 23033–23049. (10.1029/1999JB900213)
26. Galgana GA, Grosfils EB, McGovern PJ. 2013 Radial dike formation on Venus: Insights from models of uplift, flexure and magmatism. *Icarus* **225**, 538–547. (10.1016/j.icarus.2013.04.020)
27. Ernst RE, Buchan KL. 1997 Giant radiating dyke swarms: their use in identifying pre-Mesozoic large igneous provinces and mantle plumes. *Geophysical Monograph-American Geophysical Union* **100**, 297–334. (10.1029/GM100p0297)
28. Bolchover P, Lister JR. 1999 The effect of solidification on fluid–driven fracture, with application to bladed dykes. *Proceedings of the Royal Society of London. Series A: Mathematical, Physical and Engineering Sciences* **455**, 2389–2409. (10.1098/rspa.1999.0409)
29. Reverso T, Vandemeulebrouck J, Jouanne F, Pinel V, Villemin T, Sturkell E, Bascou P. 2014 A two-magma chamber model as a source of deformation at Grímsvötn Volcano, Iceland. *Journal of Geophysical Research: Solid Earth* **119**, 4666–4683. (10.1002/2013JB010569)
30. Krassilnikov A. 2002 Tectonic structure, classification, and evolution of arachnoids on Venus: Preliminary results. *Solar System Research* **36**, 374–402. (10.1023/A:1020411404593)
31. Delaney PT, Pollard DD. 1982 Solidification of basaltic magma during flow in a dike. *American Journal of Science* **282**, 856–885. (10.2475/ajs.282.6.856)
32. Rubin AM. 1993 On the thermal viability of dikes leaving magma chambers. *Geophysical Research Letters* **20**, 257–260. (10.1029/92GL02783)
33. Lister JR. 1994a The solidification of buoyancy-driven flow in a flexible-walled channel. Part 1. Constant-volume release. *Journal of Fluid Mechanics* **272**, 21–44. (10.1017/S0022112094004362)
34. Lister JR. 1994b The solidification of buoyancy-driven flow in a flexible-walled channel. Part 2. Continual release. *Journal of Fluid Mechanics* **272**, 45–66. (10.1017/S0022112094004374)
35. Detournay E. 2016 Mechanics of hydraulic fractures. *Annual review of fluid mechanics* **48**, 311–339. (10.1146/annurev-fluid-010814-014736)
36. Peirce A. 2016 Implicit level set algorithms for modelling hydraulic fracture propagation. *Philosophical Transactions of the Royal Society A: Mathematical, Physical and Engineering Sciences* **374**, 20150423. (10.1098/rsta.2015.0423)
37. Dontsov E. 2016 Propagation regimes of buoyancy-driven hydraulic fractures with solidification. *Journal of Fluid Mechanics* **797**, 1–28. (10.1017/jfm.2016.274)
38. Taisne B, Tait S. 2011 Effect of solidification on a propagating dike. *Journal of Geophysical Research: Solid Earth* **116**. (10.1029/2009JB007058)
39. Sigmundsson F, Hooper A, Hreinsdóttir S, Vogfjord KS, Ofeigsson BG, Heimisson ER, Dumont S, Parks M, Spaans K, Gudmundsson GB et al.. 2015 Segmented lateral dyke growth in a rifting event at Bardharbunga volcanic system, Iceland. *Nature* **517**, 191–195. (10.1038/nature14111)
40. Chanceaux L, Menand T. 2016 The effects of solidification on sill propagation dynamics and morphology. *Earth and Planetary Science Letters* **442**, 39–50. (10.1016/j.epsl.2016.02.044)
41. Adachi JI, Detournay E, Peirce AP. 2010 Analysis of the classical pseudo-3D model for hydraulic fracture with equilibrium height growth across stress barriers. *International Journal of Rock Mechanics and Mining Sciences* **47**, 625–639. (10.1016/j.ijrmms.2010.03.008)
42. Lister JR. 1990 Buoyancy-driven fluid fracture: similarity solutions for the horizontal and vertical propagation of fluid-filled cracks. *Journal of Fluid Mechanics* **217**, 213–239. (10.1017/S0022112090000696)
43. Berry MJ, Fuchs K. 1973 Crustal structure of the Superior and Grenville provinces of the Northeastern Canadian Shield. *Bulletin of the Seismological Society of America* **63**, 1393–1432. (10.1785/BSSA0630041393)
44. Sigmundsson F, Parks M, Geirsson H, Hooper A, Drouin V, Vogfjörd KS, Ófeigsson BG, Greiner SH, Yang Y, Lanzi C et al.. 2024 Fracturing and tectonic stress drive ultrarapid magma flow into dikes. *Science* **383**, 1228–1235. (10.1126/science.adn2838)
45. Tada H, Paris P, Irwin GR. 2000 *The Stress Analysis of Cracks Handbook; Third edition* vol. 130. New York: ASME Press. (10.1115/1.801535)
46. Lecampion B, Zia H. 2019 Slickwater hydraulic fracture propagation: near-tip and radial geometry solutions. *Journal of Fluid Mechanics* **880**, 514–550.
47. Yang BH, Joseph DD. 2009 Virtual nikuradse. *Journal of Turbulence* **10**, 1–28. (10.1080/14685240902806491)

48. Dontsov E, Peirce A. 2017 Modeling planar hydraulic fractures driven by laminar-to-turbulent fluid flow. *International Journal of Solids and Structures* **128**, 73–84. (10.1016/j.ijsolstr.2017.08.016)
49. Zolfaghari N, Dontsov E, Bunger A. 2018 Solution for a plane strain rough-walled hydraulic fracture driven by turbulent fluid through impermeable rock. *International Journal for Numerical and Analytical Methods in Geomechanics* **42**, 587–617. (10.1002/nag.2755)
50. Morgan WJ. 1965 Gravity anomalies and convection currents: 1. A sphere and cylinder sinking beneath the surface of a viscous fluid. *Journal of Geophysical Research* **70**, 6175–6187. (10.1029/JZ070i024p06175)
51. Molnar P, England PC, Jones CH. 2015 Mantle dynamics, isostasy, and the support of high terrain. *Journal of Geophysical Research: Solid Earth* **120**, 1932–1957. (10.1002/2014JB011724)
52. Koch DM, Manga M. 1996 Neutrally buoyant diapirs: A model for Venus coronae. *Geophysical Research Letters* **23**, 225–228. (10.1029/95GL03776)
53. Brotchie J, Silvester R. 1969 On crustal flexure. *Journal of Geophysical Research* **74**, 5240–5252. (10.1029/JB074i022p05240)
54. Timoshenko S, Woinowsky-Krieger S et al.. 1959 *Theory of plates and shells* vol. 2. McGraw-hill New York.
55. Sleep NH. 2007 Origins of the plume hypothesis and some of its implications. *Geological Society of America Special Paper* **430**, 29–45. (10.1130/2007.2430(02))
56. Giordano D, Russell JK, Dingwell DB. 2008 Viscosity of magmatic liquids: a model. *Earth and Planetary Science Letters* **271**, 123–134. (10.1016/j.epsl.2008.03.038)
57. BGS. 2007 . Bedrock geology map UK north sheet (north of National Grid line 460 km N) 5th Edition, British Geological Survey, scale 1:625,000.
58. Basilevsky A. 2008 . Geologic map of the Beta Regio quadrangle (V-17), Venus, U.S. Geological Survey Scientific Investigations Map 3023.
59. Hou G, Kusky T, Wang C, Wang Y. 2010 Mechanics of the giant radiating Mackenzie dyke swarm: a paleostress field modeling. *Journal of Geophysical Research: Solid Earth* **115**.
60. Buchan KL, Ernst RE. 2019 Giant circumferential dyke swarms: catalogue and characteristics. *Dyke swarms of the world: A modern perspective* pp. 1–44.
61. Gee B, Gracie R. 2024 The influence of turbulence and inertia in radial fracture flow. *Journal of Fluid Mechanics* **981**, A1. (10.1017/jfm.2023.989)
62. Zia H, Lecampion B. 2017 Propagation of a height contained hydraulic fracture in turbulent flow regimes. *International Journal of Solids and Structures* **110**, 265–278. (10.1016/j.ijsolstr.2016.12.029)
63. Crouch SL, Starfield A. 1982 *Boundary element methods in solid mechanics: with applications in rock mechanics and geological engineering*. Allen & Unwin.
64. Pollard DD, Holzhausen G. 1979 On the mechanical interaction between a fluid-filled fracture and the Earth's surface. *Tectonophysics* **53**, 27–57. (10.1016/0040-1951(79)90353-6)
65. Zia H, Lecampion B. 2020 PyFrac: A planar 3D hydraulic fracture simulator. *Computer Physics Communications* **255**, 107368. (10.1016/j.cpc.2020.107368)

royalsocietypublishing.org/journal/rspa Proc R Soc A 0000000

Supplementary material for Megadyke propagation down dynamic topography

Tim Davis[1,2], Yuan Li[2], Adina E. Pusok[2] and Richard F. Katz[2]

S.1. Empirical formulation for turbulent flow

In this section we introduce the empirically calibrated closure we use to model turbulent flow within the dyke.

(a) Momentum conservation in incompressible fluid flow

The mean fluid velocity, U, in the x-direction, within a 2D slot of width w_f in the y-direction, is given by $U = q/w_f$, where q represents the 2D volume rate in units of m^2/s. The width-averaged conservation of momentum for incompressible fluid flow in the crack is

$$\frac{\partial q}{\partial t} + \frac{\partial}{\partial x}\left(\psi(Re)\frac{q}{w_f}\right) = -\frac{w_f}{\rho_f}\frac{\partial \bar{p}}{\partial x} - \frac{1}{2}F\left(\frac{4}{3}Re, \frac{w_R}{w_f}\right)\frac{q^2}{w_f^2}. \tag{S1}$$

The terms, in the order they are displayed, represent the transient, convective term, pressure term, and friction term [61]. The terms on the left-hand side are collectively referred to as 'inertial terms'. The gradient in the pressure term $\partial\bar{p}/\partial x = \partial p/\partial x + \rho_f g \partial h/\partial x$ depends on the fluid pressure gradient $\partial p/\partial x$ and the component of the body force that acts along x. The latter is non-zero only if the LNB is tilted with respect to gravity.

This equation contains two non-dimensional terms that relate to the flow regime. The first is the momentum correction factor, $\psi(Re)$, which accounts for the increased total momentum due to the non-uniform velocity profile across the aperture [61]. The second term is the friction factor, F, which represents the momentum dissipation caused by fluid viscosity and turbulence. In laminar flow, dissipation arises solely from viscous shear forces, while in turbulent flow, it results from both viscous shear and the formation of turbulent eddies. Determining the friction factor in the turbulent regime requires an empirical relationship, as F depends on the Reynold's number and surface roughness. For this study, we employ the fluid-flow model of Yang and Dou [47], selected for its accurate prediction of friction factors across laminar, transitional, and fully turbulent regimes. We further incorporate a slot-shape correction factor, $(4/3)Re$, based on the approach by Lecampion and Zia [46].

(b) Neglecting inertial effects, Darcy-Weisbach equation

For flow in a thin channel or fracture, the inertial effects on the left-hand side of the momentum conservation equation are significant only over extremely short time scales, primarily near the fluid source, for both radial and height-constrained fractures [61,62]. Furthermore, the empirical friction factor is derived from steady, unidirectional, and fully developed flow, making it unsuitable for modelling unsteady flow conditions. Considering the momentum equation without inertial effects, only frictional effects remain, leading to the phenomenological Darcy-Weisbach equation for flow speeds dominated by frictional effects

$$-\frac{\partial \bar{p}}{\partial x} = F\left(\frac{4}{3}Re, \frac{w_R}{w_f}\right)\frac{\rho_f}{2}\frac{U^2}{D}, \tag{S2}$$

which depends on D, the ratio of the area of the crack to the wetted perimeter which for a fracture is approximately $2w_f$ [48]. This also includes the mean flow speed, U which relates to q via $q = Uw_f$. For laminar flow, the friction coefficient F reduces to $F = 96/Re$. Substituting this into Equation (S2) provides the lubrication-theory result for mean flow through a slot

$U = -\partial\bar{p}/\partial x \times w_f^2/\eta'$. Substituting D for the fracture geometry and q results in

$$-\frac{\partial \bar{p}}{\partial x} = F\left(\frac{4}{3}Re, \frac{w_R}{w_f}\right)\frac{\rho_f}{4}\frac{q^2}{w_f^3}. \tag{S3}$$

(c) Solving for flow rate q

We compute the residual ϵ to measure the difference between the computed flux and the flux derived from the Darcy-Weisbach equation

$$\epsilon = q - \sqrt{\frac{\partial \bar{p}}{\partial x}\frac{4w_f^3}{F\rho_f}}. \tag{S4}$$

Root finding ϵ is a means to solve the non-linear equation (S3) for flow rate q in the fracture.

(d) Roughness and flux

Using our pseudo-3D method, we model flow through cross-sectional openings of the dyke. When modelling turbulent flow, we introduce a roughness parameter w_R that affects the resulting flow speeds in our empirical turbulent-flow model. All other parameters that influence turbulent flow are already incorporated into our dyking model when we assume laminar Poiseuille flow.

We test how the roughness parameter w_R influences turbulent flux through a dyke cross-section by examining empirical relations for turbulent flow speed in a dyke with varying roughness and pressure gradients, compared to a dyke with no roughness under laminar flow conditions (3.2). By systematically varying the pressure gradient across this cross-section, we find that when the wall roughness w_R is less than one-hundredth of the dyke's maximum width, there is no discernible difference turbulent of the 3D flux ($\hat{Q}$) for any value of Reynolds number *Re*from Eq. (2.7).

S.2. Exploring overlooked elements of the model

(a) Crustal stiffness, domal uplift and tangential stresses

Our model of crustal uplift above a hotspot head in sec. 2(c) assumes no stiffness of the overlying plate. Here we test how plate stiffness affects this solution for domal uplift. To test this we use the elastic solution for the deflection of a thin, linearly elastic shell overlying a viscous medium in spherical coordinates, where the shell is loaded vertically by a cylindrical pressure source [53]. We apply this solution through superposition, integrating the vertical stress profiles due to the rising plume head from [50] to construct the distributed load at the base of the crust. The inflection point of both the stress and the zero-stiffness uplift curve in Eq. (2.11) is

$$\tilde{x} = b\sqrt{\frac{2}{3}}. \tag{S1}$$

Flexural rigidity of the shell, D, and the radius of relative stiffness L, are introduced

$$\begin{aligned} D &= \frac{E'\varsigma^3}{12}, \\ L^4 &= \frac{D}{\rho_m g + (E\varsigma/\chi^2)}. \end{aligned} \tag{S2}$$

where ς is the crust's elastic thickness and χ is the planet's radius. For Earth and Venus, the second term in the denominator of L is negligible, and for a crust 10–75 km thick, and a crustal stiffness of 10–100 GPa values of L are 1×10^4 to 1×10^5. Figure S2 shows how the domal uplift changes as the crustal stiffness increases. For a plume head radius b between 250 and 500 km, this results in b/L ratios between 2.5 and 50. Thus, it appears that crustal stiffness is negligible for this study of loading due to a plume head, as the change in h for these b/L values is negligible.

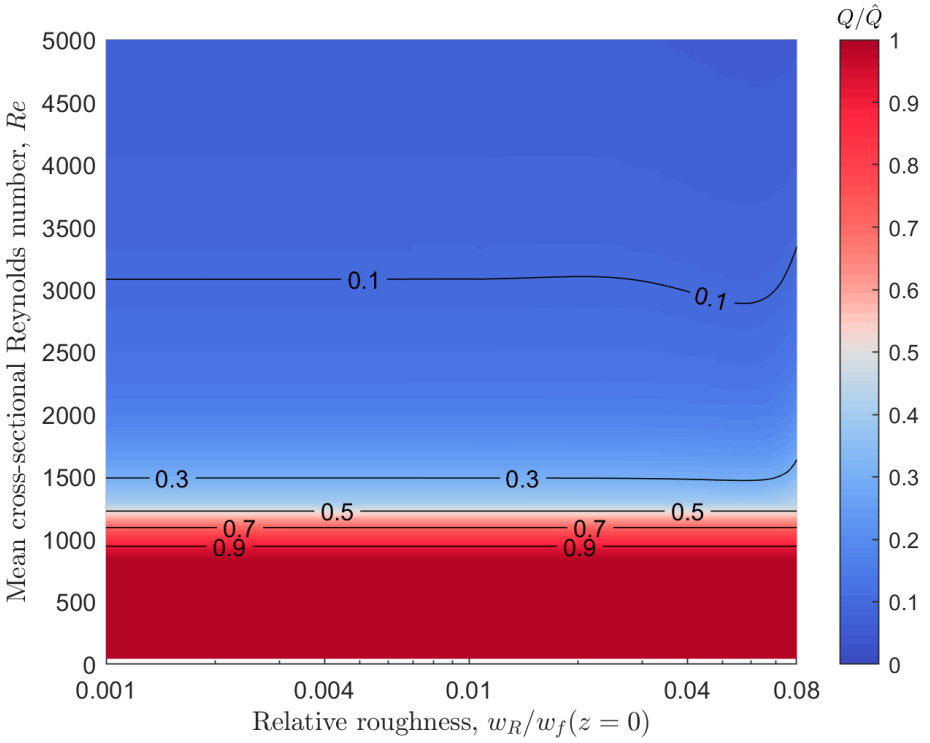

Fig. S1. Relative roughness of the fracture walls vs the average Reynolds number for a dyke with cross-section (3.1). The 3D turbulent flux Q is compared to its laminar equivalent $\hat{Q}$ (3.2).

In the model, tangential stresses due to bending of the crust are assumed to be negligible along the dyke's LNB. Using thin plate theory, tangential stresses are zero at the neutral plane, corresponding to the centre of the crust, and increase or decrease linearly to a maximum value at the plate's top and base. The dyke is assumed to be located near the neutral plane, given the large vertical extents of the modelled dykes relative to typical crustal thicknesses. Thin plate theory is used to quantify bending stresses at the ground surface for the given parameters and swell model, revealing that the maximum tensile stress occurs between $x = 0$ and b and is the same magnitude as p_0. This effect is reduced if the dyke is deeper in the crust. Additionally, if plate stiffness is included in the calculation of domal uplift, this further decreases these stresses, as observed for the uplift (Figure S2).

(b) Half-space effects

Dykes remain close to the free surface during lateral propagation, with the depth to the upper tip typically less than the total dyke height [16]. Do the effects of the free surface need to be included in our model? The inclusion of free surface effects in the model is tested by examining how the half-space geometry affects the vertical cross-sectional shape, size, and internal pressure, which in turn influences the flux via Eq. (2.6). For the half-space cross-section, we simultaneously solve for two unknowns (p_f and c) through a constrained solution procedure. These two unknowns are the fluid pressure p_f and the dyke's centre height c above the LNB. Prescribing the dyke height $\hat{a}$, we require that the condition of zero toughness at both tips ($K_I = 0$) is matched. The free surface is denoted as d, the vertical distance from the LNB. Common elastostatic integration techniques for fractures are used to simulate opening distributions, ensuring that both the fracture walls and the ground surface are free from normal and shear tractions [23,63,64].

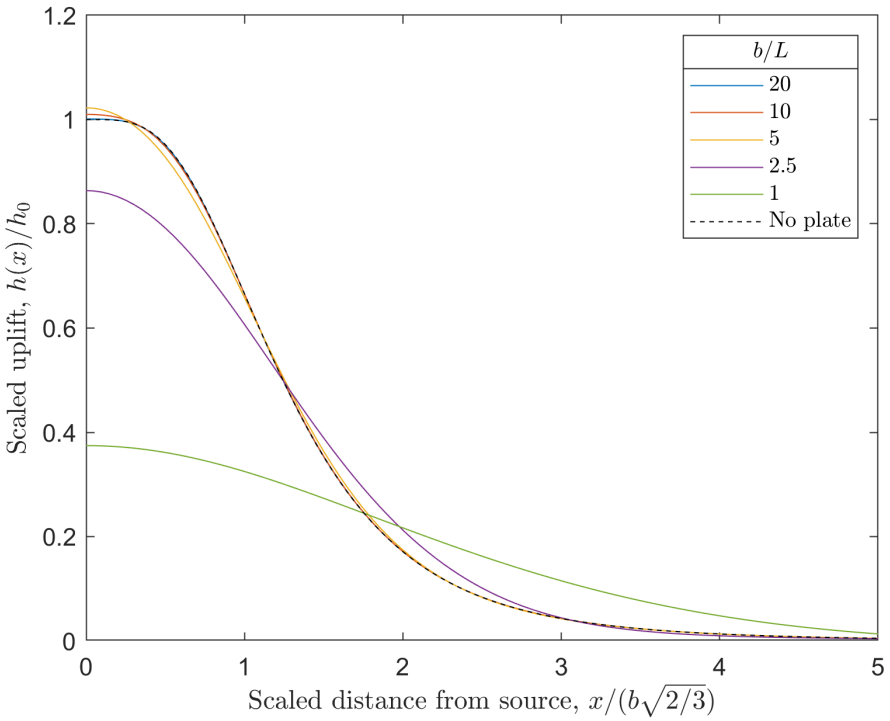

Fig. S2. Changes to the domal uplift profile as the bending length (S2) increases relative to the plume head radius. x is scaled by (S1) and h by (2.11).

We show the results in Figure S3, setting toughness to zero. In this instance, even as the dyke tip approaches the free surface, the fluid pressure p_f changes by a maximum of 15%. The dyke's centre rises above the LNB only slightly (by length c). This is because the presence of the free surface increases the stress intensity at both tips of the dyke, with the upper tip experiencing greater intensities. However, the gravitational effects due to the increasing crustal density are so strong that even slight movements of the dyke's centre relative to the LNB are sufficient to counter this asymmetry, forcing the stress intensity at both tips to equalise. This results in vanishingly small differences in the opening distribution. This shows that even if the dyke is close to the free surface, it will have a minimal effect on the results of our simulations.

Figure S4 illustrates dykes that have breached the free surface, with the fracture closed at the lower tip ($K_I(z=-a)=0$). Since the free surface provides no fracture constraint, a second constraint is required to solve the system. We obtain this constraint by requiring the fluid area of the portion below the free surface match the corresponding below-surface area from the full-space solution, $A_f(z-d<0)=\hat{A}_f(z-d<0)$.

In this configuration, the dyke's centre is displaced below the LNB, and the general shape deviates more significantly from the full-space solution than the dykes shown in Figure S3. The opening is particularly pronounced at the free surface.

The dyke profiles shown represent stable states under these conditions. For the tallest dyke displayed, 25% of the initial full-space fluid area $\hat{A}_f$ has been lost (erupted). Despite this substantial eruption and the geometrical deviations, the full-space width profile remains a good leading-order approximation for the portion of the fluid that is retained within the crust.

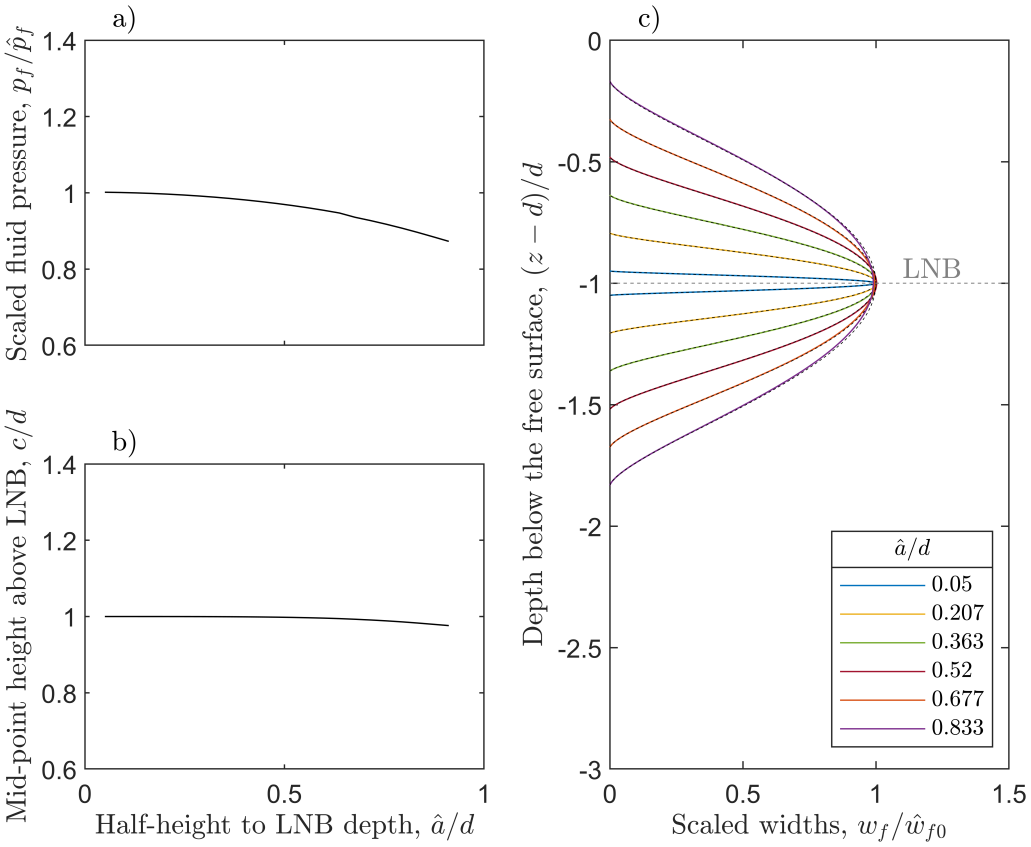

Fig. S3. Near-surface effects on dyke geometry compared to a full-space solution. Calculations show a dyke in a crust with linearly increasing density as it approaches the free surface. **Panel a & b** (Pressure and offset): The full-space solution for the fluid pressure ($\hat{p}_f$) and dyke mid-point are perturbed to satisfy the fracture criterion $K_I(z=\pm a)=0$ at the dyke tips. This results in minimal deviations in the scaled fluid pressure ($p_f/\hat{p}_f$) (a) and requires a minor offset of the dyke's centre above the LNB (c/d) (b). **Panel c** (Dyke Geometry). The scaled dyke widths ($w_f/\hat{w}_{f0}$) for various scaled half-heights ($\hat{a}/d$) show minimal deviation from the analytical full-space width (dashed black lines, $\hat{w}_f$), indicating the dyke geometry is largely unperturbed.

S.3. Comparison of a full-3D to pseudo-3D simulation of lateral dyke propagation

Figure S5 presents a comparison between the results obtained from PyFrac, the fully coupled 3D simulator of Zia *et al.* [65], and our approximate, pseudo-3D simulator. The boundary conditions differ between the two: PyFrac requires a constant flux at the source, while our simulator uses a constant-pressure source condition. In the PyFrac simulation, fluid injection at $x=0$ was avoided to prevent flow out of the domain to the left. We set the flux to the value described by Eq. (S5) and the injection point to the inflection point of the uplift curve $\tilde{x}/2$. Despite these differences, the shape and propagation speed of the dyke are comparable.

It is worth noting that while PyFrac offers a more comprehensive model, it has certain limitations for our specific application. PyFrac's simulations are slower, making multiple runs intractable, and it currently only supports constant-flux boundary conditions. It lacks a fluid-solidification law and cannot adequately simulate tip blockage or handle gravitational effects and leak-off laws simultaneously. For comparison, we have deactivated any physical processes in our

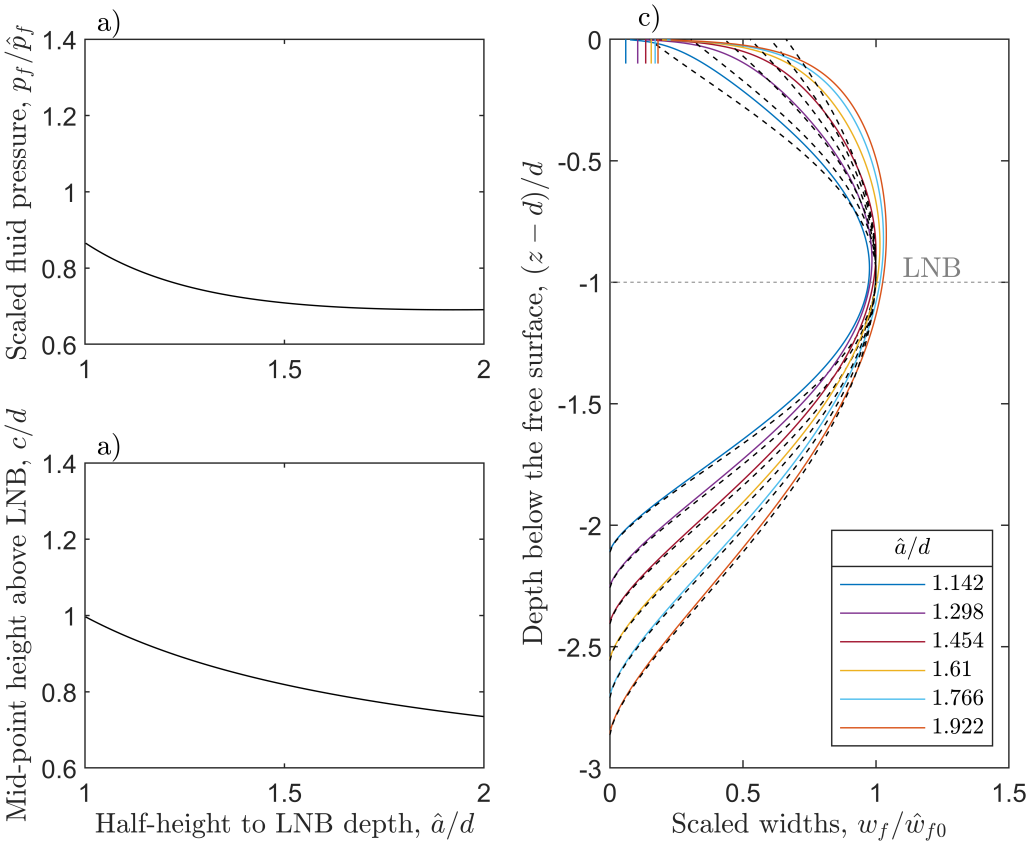

Fig. S4. This figure is a modified version of figure S3, showing dykes in a crust of linearly increasing density that have breached the free surface. **Panel c** shows vertical lines which are the opening at the free surface. Dashed black lines are the analytical full-space width $\hat{w}_f$.

model that PyFrac cannot simulate. Although PyFrac excels in the scenarios it is designed for, these constraints led us to develop our own simulator for this study.

S.4. Technical details of the model: solidification and cross-sectional singularity regularisation

(a) Calculating lambda (λ)

Lambda (λ) is a dimensionless constant that characterises the growth rate of the solidified magma layer adjacent to a propagating dyke. It is determined by the equation

$$\pi^{1/2}\lambda e^{\lambda^2}\,\mathrm{erfc}(-\lambda) = \frac{C_p(T_s - T_\infty)}{L_m}, \tag{S1}$$

where C_p is the specific heat of the solidified magma (J kg^{-1} K^{-1}), T_s is the solidification temperature of the magma (K), T_∞ is the background temperature of the host rock (K), and L_m is the specific latent heat of magma solidification (J kg^{-1}). The thermal diffusivity, κ, which has units of m^2/s, also plays a role in determining the growth rate, although it is not directly included in the equation for λ. The equation essentially balances the energy released during solidification with the heat that needs to be conducted away, defining the thickness of the chill layer formed against the dyke.

Fig. S5. A comparison of a fully 3D numerical simulator (PyFrac) to our pseudo-3D simulation of a laterally propagating dyke. Simulation properties are detailed in §3(a). Note the maximum LNB uplift h_0 is 1 km but has been exaggerated here to highlight its distortion **Panel a** shows a simulation using the full 3D numerical simulator [65]. The dyke is driven by a volumetric flux Q from the blue dot with a value determined by (S5). **Panel b** shows a corresponding simulation using our pseudo-3D model, with a pressure boundary at the source $x = 0$. **Panel c** compares the lateral tip speeds of the two models.

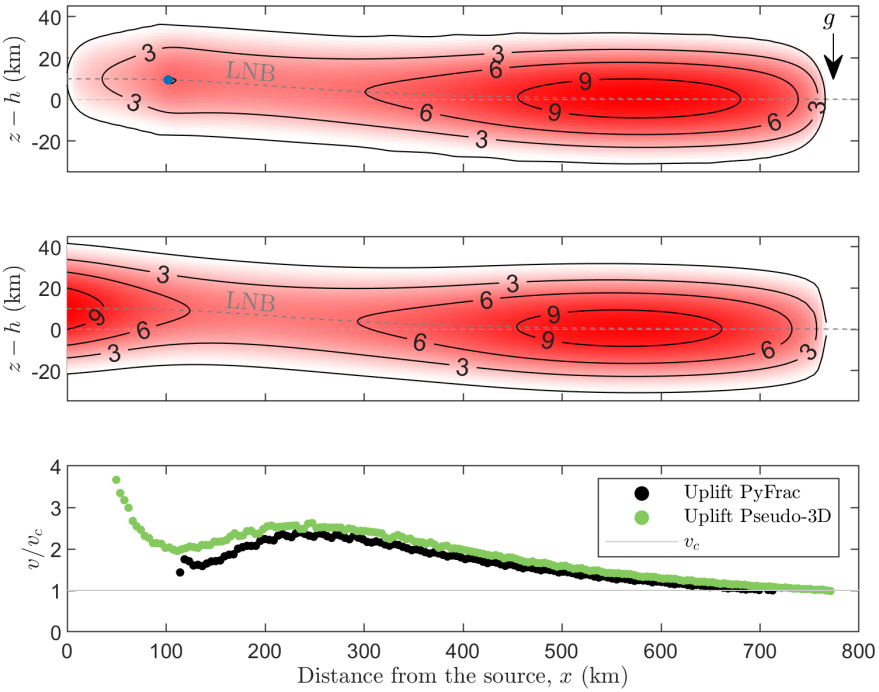

(b) Minimum dyke height in cross-section

As described in Bolchover & Lister [28], when K_c is non-negligible, p_f is singular as a approaches zero. Integrating (2.3), valid values of a are above

$$a^* = \left(\frac{K_c^2}{(Rg)^2 \pi} \right)^{1/5}. \tag{S2}$$

Therefore inverting for a using values of A_f smaller than

$$A_f^* = \frac{9}{4E'} \left(\frac{K_c^8 \pi}{(Rg)^3} \right)^{1/5}, \tag{S3}$$

is invalid. In our model when $A_f < A_f^*$, the dyke height is set to a^* (S2) and the dyke width is scaled by

$$w_f^* = \frac{A_f}{A_f^*} w_f. \tag{S4}$$

This satisfies the condition that the opening matches the area within the element. This approximation no longer meets the condition of $K_I = K_c$ at the tips. The centre-line pressure p_f at $z = 0$ is scaled in the same way. In our presented results we have verified this only occurs in the tip portion of the dyke as it grows vertically in its initial stages.

(c) Domal uplift and turbulence

Figure S6 is a modified version of Figure 5c that describes how pressure influences dyke lengths in the presence of domal uplift, illustrating the impact of turbulent fluid flow on final dyke length. Turbulence causes an increase in the pressures required to cause the dyke to propagate over the swell size, which, once exceeded, causes a jump in length, tending towards length $2b$. After this, the pressure-to-length scaling is similar to the case with laminar fluid flow. We note that including cross-sectional solidification does not significantly influence these results.

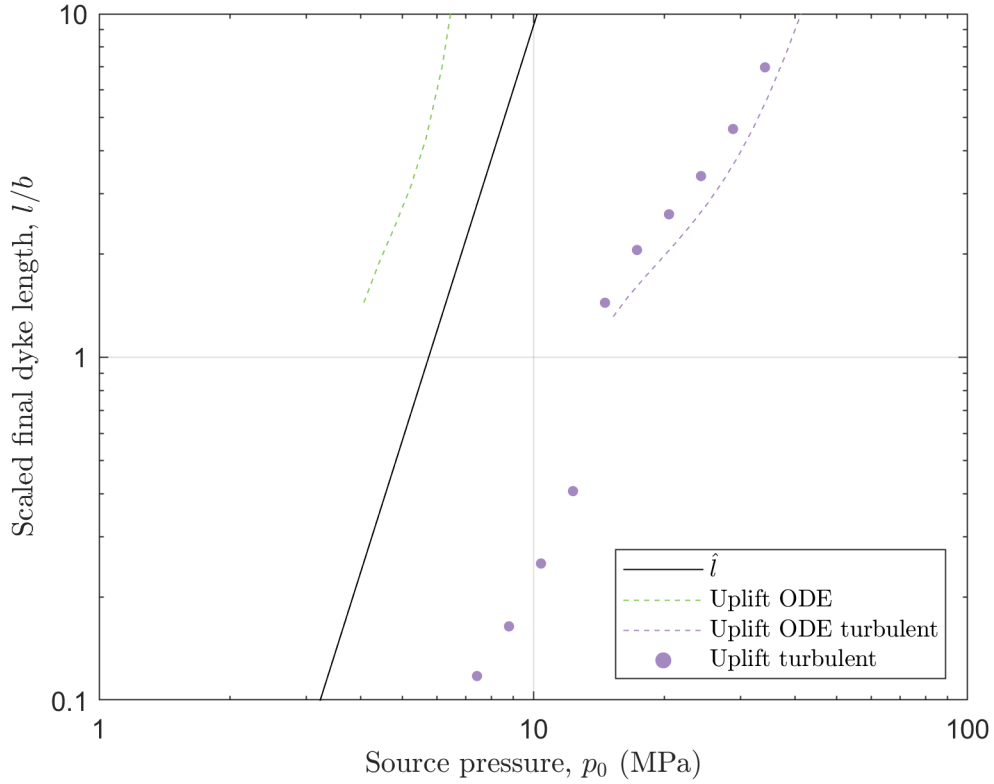

Fig. S6. Source pressure dependence vs dyke length, including the effect of turbulence. Note the increase in dyke length to that of the swell size, when the pressure is large enough, compared to the laminar case (Fig. 5).

S.5. Inclusion of solid stresses in cross-section

Here we investigate the influence of the spatial distribution of solidified material inside the crack on the centreline pressure and the crack opening profile. Our primary goal is to test the hypothesis that the details of this distribution have a negligible effect on the key transport variables: gradients in centreline pressure (which drive lateral flow (2.2)) and the integral of the cube of the fluid width (which controls the lateral flux (2.8)).

As a crack grows vertically (in the z-direction), solid material accumulates on the walls (solid thickness $w_s(z)$). The thickness $w_s(z)$ at any height depends on the contact time (δt) between the fluid and the wall. In the main text we assume that tracking solidified area A_s lost to solidification in each cross-section is adequate; i.e., we assume that the solid material's distribution has a negligible influence on the final solution. However, this method neglects the variation of normal stress along the contact between the fluid and newly frozen solid. Here we test our assumption by comparing our method to a model where we include the normal stress transmitted to the fluid through the solidified layer on the walls as the solid material deforms the host rock. We show this more detailed calculation has a negligible influence on our results.

(a) Modelling solid stress $p_s(z)$

To account for the vertical distribution of solid stress, we rewrite the total excess pressure p from (2.2) of the main text as

$$p^*(x,z,t) = p_f(x,t) + p_s(x,z,t) - Rgz^2/2, \tag{S1}$$

where $p_s(x,z,t)$ is the stress contribution arising from the solidified width profile $w_s(x,z,t)$. Different functional forms of w_s can result in distinct stress profiles $p_s(z)$, even if they yield the same total solidified area A_s.

To determine the stress distribution $p_s(z)$ due to a given solid width profile $w_s(z)$, we use a displacement discontinuity method. We discretize the dyke into n vertical segments, each having a displacement discontinuity with opening w_s. We then sum the contributions from all segments to compute the stress p_s along z (computed at segment centres to avoid singularities [63]).

Once the total pressure distribution p^* is known, we replace p with p^* in the elasticity equations ((2.3)–(2.5)) to solve for the full crack width w and total area A.

(b) Test for the influence of the solid distribution

We now test whether explicitly accounting for the vertical distribution of solid stress significantly changes the solution as compared to our simplified method.

(i) Method

We analyse a single cross-section using the following steps:

(i) Initial state. Start with a crack defined by our default parameters (Table 1).
(ii) Fluid inflow. Add extra fluid area so the total area is 150% of the initial area (representing inflow from a time-step).
(iii) Solid growth. During this time-stage, a solidified layer grows. We test two growth scenarios:
- Solid area A_s is $\approx 4\%$ of the initial fluid area (based on the longest wall contact time from Fig. 3b).
- Solid area A_s is equal to the fluid area that enters the crack.

(iv) Solid stress. Compute the vertical distribution of solid stress in p^*.
(v) Final area. Calculate the fluid-filled area A_f by subtracting the solid growth area A_s from the total cross-sectional area.

(vi) Boundary conditions. Solve for the dynamic fluid pressure p_f that satisfies the given boundary conditions and the required fluid area A_f.
(vii) Comparison. Compute the total centreline pressure $p^*(z=0)$ and width integral for different scenarios.

We test the following three vertical solid distributions, ensuring the total solidified area A_s is identical in each:

(i) No solid stress distribution. This is the method outlined in the main text. We assume $p_s = 0$, meaning the solid material has no influence on the pressure or rock deformation. The total centreline pressure is $p^*(z=0) = p_f$.
(ii) Constant solid width. Prescribe a uniform solid thickness in z. This creates a solid stress distribution like a dislocation with a constant opening.
(iii) Variable solid width. Prescribe a solid thickness that varies with height, following a scaled form of the fluid width, equation (3.1).

We solve each scenario for two different boundary conditions:

- A crack with blocked upper and lower tips of a fixed height (Fig. 2e).
- A vertically propagating crack (Fig. 2d).

(c) Fixed height, vertically blocked crack

Here the crack height is fixed and we solve for the magnitude of the dynamic pressure p_f that results in our known fluid area A_f. The centreline pressure $p^*(z=0)$ is identical for all three scenarios, independent of the solid distribution ($w_s(z)$). Crucially, the integral $\int_{-a}^{a} w_f^3 \mathrm{d}z$ is also the same, despite differences in the resulting fluid width profile $w_f(z)$. These results hold even when the solid growth area is increased to match the fluid area entering the cross-section.

(d) Vertically propagating crack

In this scenario, the constraints are that the fracture toughness K_c is satisfied at crack tips and the crack fluid area is A_f. The unknowns to solve are the crack height a and the magnitude of the dynamic pressure p_f. Despite differences in the final crack height and opening profile between the three scenarios, the key quantities—the centreline pressure $p^*(z=0)$ and the flux integral $\int_{-a}^{a} w_f^3 \mathrm{d}z$—vary by less than 1%. Again, increasing the area of solid growth to match the fluid coming into the cross-section results in no change to the differences between the quantities.

(e) Summary

We conclude that the explicit spatial distribution of solid material within a cross-section has a negligible impact on the quantities that govern lateral flow. Although the cross-sectional geometry differs quantitatively between solid distributions, the centreline pressure $p^*(z=0)$ (which drives lateral flow) and the integral $\int_{-a}^{a} w_f^3 \mathrm{d}z$ (which controls the lateral flux) consistently vary by less than 1%. Therefore, for modelling lateral transport, tracking only the total solidified area A_s (as done in the main manuscript) is sufficient and justified.

S.6. Pseudo-3D simulation including the physics of solidification

Figure S7 presents the same simulation of a laterally propagating dyke as shown in Figure 3, but where tip blocking due to solidification is taken into account at both the vertical and lateral tips, as described in Sections 2(e) [28] and shown in Fig. 2d,e. When comparing the two cases that include uplift, enabling vertical blocking results in a reduction in the vertical tip height, a dyke

that is around 15% longer, and greater central dyke widths. This comparison highlights the minor impact of solidification on the form of propagating dykes.

Fig. S7. Comparison of laterally propagating dyke shapes that include tip-blockage. This figure is a modified version of Figure 3, illustrating the impact of including blockage of the vertical dyke tips §2(e).iii. The simulation properties are detailed in §3(a). This figure highlights the differences in dyke behaviour when the additional cross-sectional physical constraints are applied.

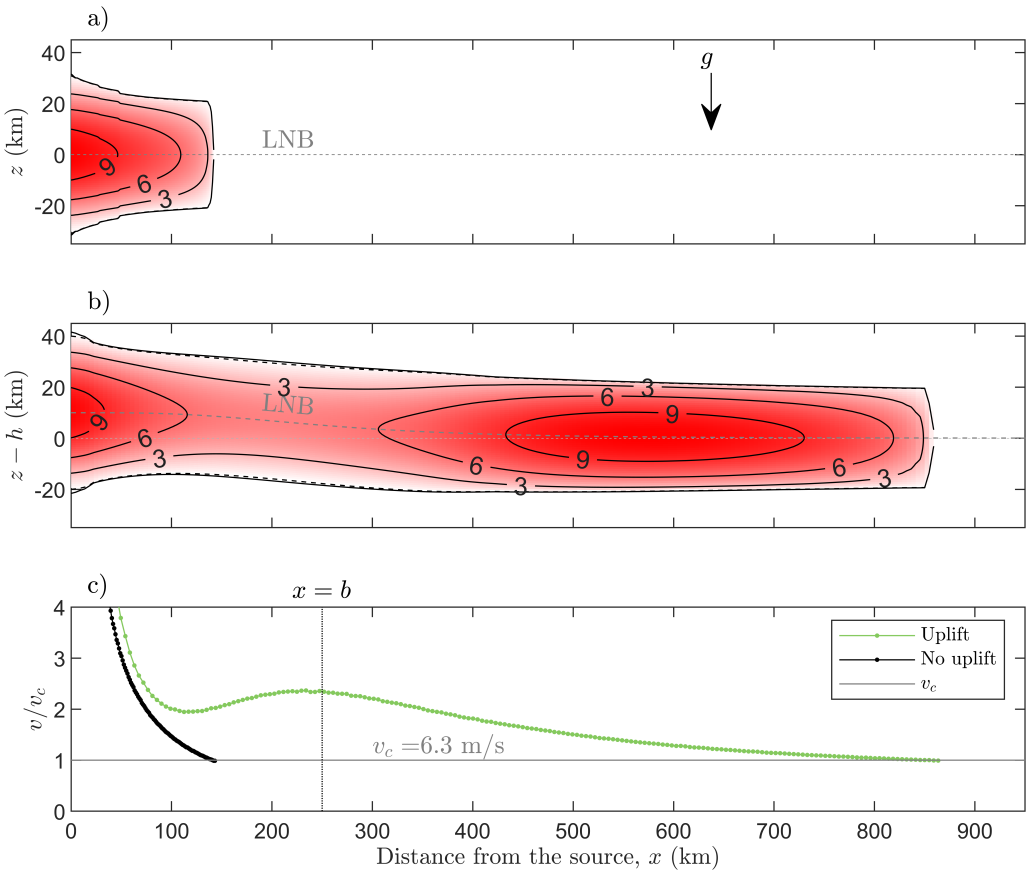

S.7. Non-dimensional ODE for dyke length over a domal uplift

An ordinary differential equation (ODE) is introduced here, based on numerical simulations showing that the 3D flux at the source, Q, quickly achieves a near constant value in time as the dyke propagates down-slope. A derivation of an approximate value for this steady Q is provided, allowing this to be rearranged into an ODE describing the dyke's tail shape and the speed of fluid flow (Fig. 6).

To understand this behaviour we

- Define the characteristic length scale. This represents the distance at which the flux, Q, stabilises and we define its magnitude at this distance.
- Develop a non-dimensional ODE. This simplified equation will describe the pressure dynamics within the dyke.

- Introduce non-dimensional constants. These constants will capture the key factors governing the final dyke length.

By analysing this non-dimensional problem, the goal is to arrive at a universal relationship as depicted in Figure S8. This plot defines the final dyke length for any combination of variables, captured by just two non-dimensional constants.

(a) Approximating the steady 3D fluid-flux at the source

Our pseudo-3D numerics show that Q tends to a constant when

$$\frac{\partial p_f}{\partial x}(x=l) \sim \rho_f g \frac{\partial h}{\partial x}(x=l), \tag{S1}$$

The left-hand side is from equation (3.3). Differentiating the uplift curve (2.11) results in

$$\rho_f g \frac{\partial h}{\partial x} = -\rho_f g \left(\frac{3780 b^6 (4h_0)/(3b) x^3}{3x^2 + 4b^2} \right)^{9/2}. \tag{S2}$$

Dropping the first term in the denominator provides an approximate weight gradient close to the source ($x \ll b$)

$$\rho_f g \frac{\partial h}{\partial x} \approx -\rho_f g \left(\frac{3780 b^6 (4h_0)/(3b) x^3}{4b^2} \right)^{9/2}. \tag{S3}$$

Comparing this to the elastic pressure gradient in the absence of topography (3.3), the distance from the source at which the two pressure gradients in (S1) are equal is

$$\hat{x} = b \left(\frac{32}{1575} \frac{p_0}{h_0 \rho_f g} \right)^{1/4}, \tag{S4}$$

substituting this distance into (3.3) to compute the pressure gradient and solving for the flux $\hat{Q}$ results in

$$\hat{Q}_0 = C \frac{(p_0^{23} h_0 \rho_f g)^{1/4}}{E'^3 (Rg)^2 b \eta'}. \tag{S5}$$

Note C is

$$C = \frac{448\pi}{45} \left(\frac{1575}{32} \right)^{1/4} \approx 83.0. \tag{S6}$$

This provides us with the approximate steady flux at the source of the dyke, which we use as a Neumann boundary condition in our ODE that follows. The mean fluid speed at the source is calculated by substituting $\hat{Q}_0$ into the equation for fluid speed (2.9).

$$\hat{v}_0 = \frac{C}{4\pi} \frac{(p_0^{15} h_0 \rho_f g)^{1/4}}{E'^2 R g b \eta'}. \tag{S7}$$

Thus, we have an approximation of a steady source flux and fluid velocity, provided the dyke stays above the critical velocity before it reaches a sufficient distance (S4).

(b) Non-dimensional ODE for the fluid pressure

We utilise this approximation of a steady source flux and assume that once developed, each cross-section has a steady flux. This allows us to derive an ODE for the lateral variation in dyke pressure and shape.

We introduce the following non-dimensional variables

$$p' p_c = p_f, \qquad x' b = x. \tag{S8}$$

Rearranging $\hat{Q}$ from (3.2) for $\partial p/\partial x$ we find

$$\frac{3}{224\pi}\frac{\hat{Q}E'^3(Rg)^2\eta'}{p_f^5} = -\rho_f g\frac{\partial h}{\partial x} - \frac{\partial p_f}{\partial x}. \tag{S9}$$

Non-dimensionalising Eq. (S2) provides

$$\frac{\partial h}{\partial x'} = -\frac{h_0}{b}\frac{5040x'^3}{(3x'^2+4)^{9/2}}, \tag{S10}$$

and (S9) becomes

$$\left[\frac{3}{224\pi}\frac{\hat{Q}E'^3(Rg)^2\eta'}{p_c^5}\right]p'^{-5} = \left[\rho_f g\frac{h_0}{b}\right]\frac{5040x'^3}{(3x'^2+4)^{9/2}} - \frac{p_c}{b}\frac{\partial p'}{\partial x'}. \tag{S11}$$

Assuming the terms in square brackets balance and substituting $\hat{Q}$ with $\hat{Q}_0$ from (S5) and rearranging this we find

$$p_c = D\left(\frac{p_0^{23}}{(h_0\rho_f g)^3}\right)^{1/20}, \qquad \text{with} \quad D = \left(\frac{3C}{224\pi}\right)^{1/5}. \tag{S12}$$

Substituting p_c and dividing each term of (S11) by p_c/b provides the final non-dimensional ODE

$$\mathcal{P}\frac{\partial p'}{\partial x'} = \frac{5040x'^3}{(3x'^2+4)^{9/2}} - p'^{-5}, \tag{S13}$$

where $\mathcal{P}$ is

$$\mathcal{P} = D\left(\frac{p_0}{h_0\rho_f g}\right)^{23/20}. \tag{S14}$$

Note that we convert the pressure distribution to half-height using (3.1) in Figure 6b.

(c) Solving for the final dyke-length

Equation (S13) takes the pressure p_0 at the source as the initial condition. Once the pressure distribution from S13 is obtained, the speed along the dyke is computed using $\hat{v}$ from (3.2), as illustrated in Figure 6c. We use this mean flow as a proxy for the tip speed during lateral propagation, equating the two under the assumption that the dyke remains stable in height, flow width, and flow speed once the tip has passed. It is noted that at large x', $p \propto x^{1/6}$, $a \propto x^{1/12}$ and $v \propto x^{-1/3}$. The length of the dyke is then determined by finding where $v - v_c = 0$. Thus, the ODE can provide final lengths for a given source pressure condition (p_0). In this analysis the fluid speed v_f is of interest, as it determines the final length. Therefore, we introduce a second non-dimensional number $\mathcal{V}$

$$\mathcal{V} = \frac{C}{4\pi}\frac{K'^2(p_0^{15}h_0\rho_f g)^{1/4}}{E'^4\alpha^2 Rg\eta' b}. \tag{S15}$$

This represents the ratio of the mean fluid speed at the source once the volume rate has stabilised in the presence of uplift (S7) to the critical velocity (v_c). Larger values of $\mathcal{V}$ result in longer dykes. Figure S8 shows how the resultant dyke lengths change as a function of $\mathcal{P}$ and $\mathcal{V}$.

S.8. Regions where the topographic influence on dyke length is negligible

Figure S8 explores the non-dimensional space of $\mathcal{P}$ and $\mathcal{V}$, and shows how the predicted dyke lengths change as a function of these parameters.

Fig. S8. Predictions from ODE model (S13) of the final length of the dyke in the presence of domal uplift. Uplift is not strong enough to have an influence on length in the areas shown in white, thus in these areas the final dyke length tends to $\hat{l}$. We define these regions in supplementary material section S.8. To aid the interpretation of Figure 5, we indicate the directions travelled when h_0, p_0 and b are increased.

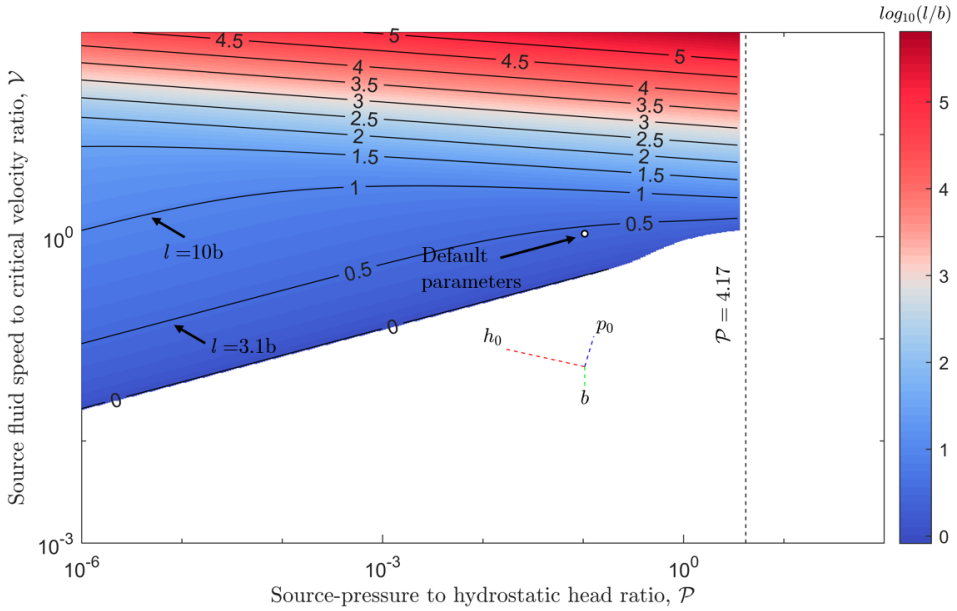

We use the ODE model to quantify when domal uplift has an observable influence on the final dyke length. The ODE provides dyke speeds assuming the source's volumetric flow rate has stabilized. The final dyke length is determined by the location where cross-sectional flow speeds drop below the critical speed. In the absence of topography, we know the final length of a dyke is $\hat{l}$, where flow is driven solely by source pressure (3.5). Since sloping topography can only assist dyke propagation by increasing lateral flow speeds, any ODE solution predicting lengths shorter than $\hat{l}$ is physically invalid—the actual dyke length must equal or exceed $\hat{l}$. Following this logic, readers can compare the lengths shown in Fig. S8 with the topography-free baseline $\hat{l}$ to identify the conditions where topographic assistance will increase dyke length.

Below we determine the region where the elastic gradient due to source pressure dominates over the topographic gradient. This is shown as the right-hand limit in Fig. S8.

(a) Where elastic pressure gradients dominate over potential energy gradients

Here we determine when the topographic pressure gradient $\approx h_0/(2b)$ is too low to significantly affect the final dyke length. When deriving the ODE, Eq. (S3) uses a simplified form of the weight gradient close to the source $x=0$. If $\tilde{x}$ is the inflection point of the uplift curve (S1) (i.e., the location of steepest topography), we propose the following condition

$$\frac{p_0}{\tilde{x}}\beta > \rho_f g \frac{\partial h}{\partial x}(x=\tilde{x}). \tag{S1}$$

This states that once the dyke length reaches the point of the maximum pressure gradient due to the topographic slope, if the pressure gradient due to elastic pressures at this location exceeds that of the slope, the slope will have little influence on the final dyke length.

In the ODE, it is assumed that the flux Q stabilizes when these two gradients are equal. However, in this case, the elastic pressure gradient $\partial p_f/\partial x$ due to the dyke is much greater than

the topographic pressure gradient, resulting in an 'uplift-induced' length from the ODE that is smaller than $\hat{l}$. Thus, if this condition is met, the dyke length will be the pressure-driven length $\hat{l}$.

The gradient (S2) at $\tilde{x}$ is

$$\rho_f g \frac{\partial h}{\partial x}(x = \tilde{x}) = \frac{70}{81}\frac{h_0}{b}\rho_f g. \tag{S2}$$

Therefore, using (S1), the conditions under which the final dyke length is dominated solely by source pressure are found by substituting this value and rearranging,

$$\mathcal{P} > 4.17. \tag{S3}$$

This bound is shown on the right hand side of Figure S8.